Table of Contents

1 Proposal Summary

1.1 REHEART Collaboration and Management Structure

In REHEART, we will focus on three main Technical Areas (TAs), TA1: Generation of all necessary hypoimmune cardiac cell types; TA2: Large scale manufacturing and biobanking of cardiac cells; TA3: Multimodal heart biofabrication and in vivo testing. During the progress, work streams will be developed for producing high quality stem cell derived cardiac specific cell types (**Fig. S1**), and nanofiber scaffolds which mimic the mechanical and chemical properties of extracellular matrix proteins (**Fig. S2**).

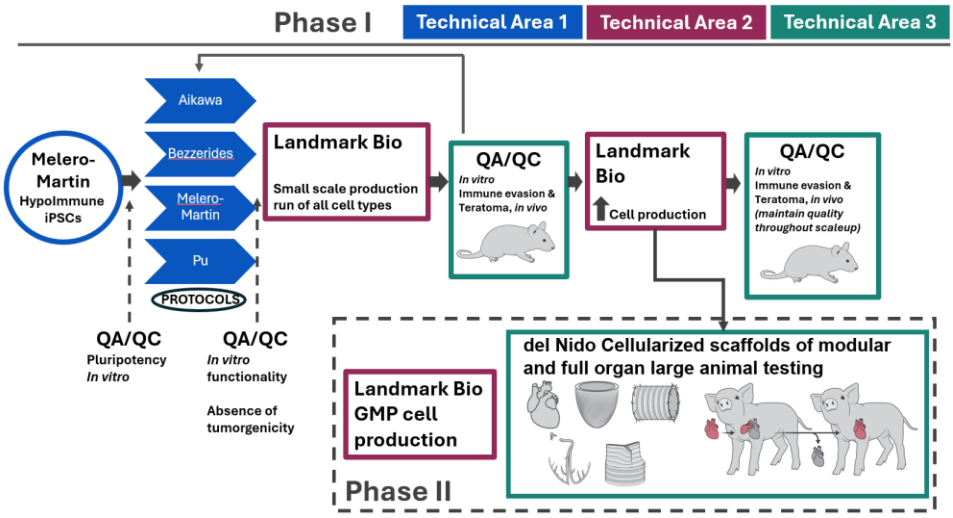

Fig. S1. REHEART Cell Development and Implantation Workflow.

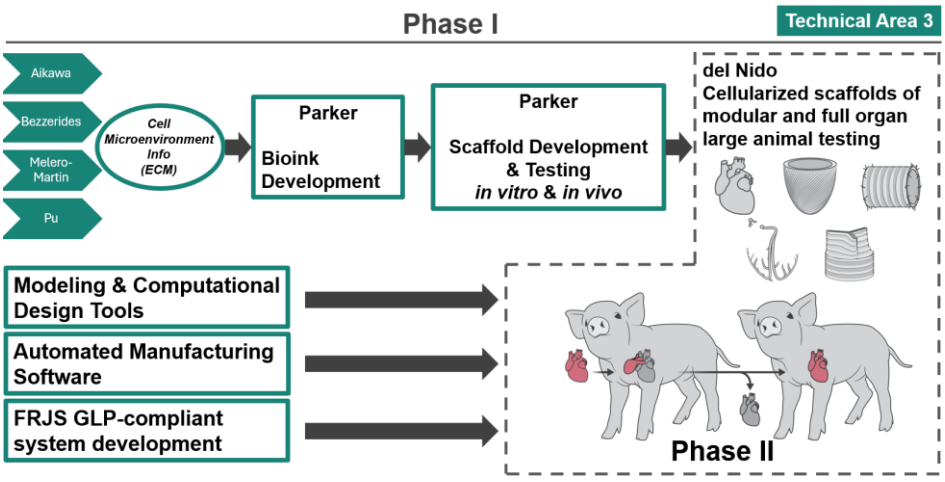

Fig. S2. REHEART Scaffold and Bioink Development and Implantation Workflow.

2 Goals and Impact:

2.1 Expanded Clinical Targets for Individual Heart Components and Full Hearts

Congenital heart disease (CHD) is the most common major birth defect, affecting approximately 1% of live births, more than 1.35 million children globally and around 40,000 annually in the United States[1–3]. Remarkably, due to significant advances in medical care and improved survival rates, the prevalence of CHD has doubled over the past two decades. Today, more than one million children are living with this condition[4–7]. Despite advancements, existing treatments for CHD often fall short due to poor long-term durability and their inability to adapt to the growth of pediatric patients. As a consequence, most children with CHD do not receive adequate care. Alarmingly, each year, fewer than 5% receive the therapy they need, and the population of children living with malfunctioning heart components continues to grow[8,9]. CHD is characterized by a wide range of defects that can involve dysfunctional inlet and outlet valves, malformed atrial and ventricular chamber walls and muscular structures, absent or hypoplastic major and minor vessels that connect the heart to the lungs, and abnormal cardiac conduction tissue, either from congenital etiologies or secondary to injury during interventions (**Table S1**). For this reason, this proposal details a modular approach to cardiac regenerative engineering to develop individual functional units, such as valves, vessels, and muscle, that the surgeon can use for patient-specific reconstructive surgery. For whole organ replacement, components will be connected using the same techniques used to insert individual units in the host heart, but instead to assemble an entire engineered heart construct as a transformative solution for children with end-stage CHD, those for whom individual component replacement is no longer viable. Through this work, we aspire not only to offer hope to patients and their families, but to move closer to a definitive cure for CHD.

CHD (Category)	CHD (Defect)	Incidence (per 10,000 births)	Prevalence* (<21 yrs old)	# of Procedures** (per year)	Mortality (% at specified year)	Reintervention (% at specified year)	References
All	**All**	**95 – 100**	**1,000,000**	**35,000 – 40,000**	**2 – 3**	**3 – 4**	10–13
Valves	Critical PS	6 – 8	~52,000	1,750	5 – 7 (25yr)	4 – 17 (10yr)	10,14–19
	MV disease	5 - 7	~37,000	1,393	6 – 19 (5yr)	19 – 39 (5yr)	20–24
	TOF/PS	4 – 5	~29,000	1,266	5 – 11 (20yr)	35 – 45 (20yr)	2,5,25,26
	Critical AS or AR	4 – 5	~24,000	1,075	12 – 21 (10yr)	38 – 50 (10yr)	2,27–29
	Complete AVC	3 – 4	~24,000	838	6 – 8 (5yr)	18 – 19 (5yr)	26,30,31
	d-TGA	3 – 4	~22,000	712	5 – 7 (25yr)	15 – 23 (25 yr)	26,32–34
	Truncus arteriosus	1 – 2	~6,000	154	20 – 23 (20yr)	21 – 26 (20yr)	2,26,35,36
	TOF/PA	1 – 2	~4,500	49	3 – 7 (2yr)	30 – 60 (2yr)	5,37,38
	TOF/APV	0.1 – 0.3	---	---	28 – 36 (10yr)	49 (20yr)	39,40
Ventricles	HLHS	3 – 4	~14,000	925	47 – 50 (15yr)	>95 (35yr)	2,26,41,42
	DORV	1 – 2	~9,000	832	6 – 11 (5yr)	25 – 45 (5yr)	2,26,43–45
	PA/IVS	1 – 2	~7,000	655	20 – 34 (25yr)	45 – 77 (25yr)	2,26,46–48
	Ebstein anomaly	0.9 – 1.0	~7,000	345	13 – 19 (<1yr)	16 – 46 (<1yr)	2,26,49–51
	Tricuspid atresia	0.7 – 0.8	~4,000	290	20 – 40 (20yr)	39 (5yr)	2,52,53
	Shone's complex	0.5 – 0.6	---	---	8 – 17 (10yr)	17 – 50 (8yr)	54–56
	Unbalanced AVC	0.3 – 0.4	---	---	25 – 34 (10yr)	38 – 70 (10yr)	57–59
Vessels	Vascular ring	1 – 3	~15,000	269	1 – 2 (10yr)	10 – 14 (10yr)	60–62
	TAPVC	0.9 – 1.0	~6,000	250	5 – 20 (15yr)	5 – 25 (15yr)	2,63–66
	TOF/PA/MAPCA	0.6 – 0.8	---	---	15 (10yr)	48 (10yr)	67,68
Conduction	Iatrogenic AVB	14 – 27% high-risk	~4,500	332	11 (5yr)	>95 (15yr)	62,69–71
Full Heart	End-stage CHD	0.9 – 1.0	~4,000	155	15 – 24 (5yr)	---	72–75
	Cardiomyopathies	0.1 – 0.2	~500	180			

Table S1: Clinical Targets for Individual Heart Components and Full Heart

Abbreviations: APV: absent pulmonary valve; AVC: atrioventricular canal; AS: aortic stenosis; AVB: atrioventricular block; CHD: congenital heart disease; DORV: double outlet right ventricle; HLHS: hypoplastic left heart syndrome; IVS: intact ventricular septum; MAPCA: major aortopulmonary collateral artery; MV: mitral valve; PA: pulmonary atresia; PS: pulmonary stenosis; TAPVC: total anomalous pulmonary venous connection; TGA: transposition of the great arteries; TOF: Tetralogy of Fallot. *Prevalence calculated from incidence and mortality rate. **Number of procedures per year calculated based on annual cases performed at BCH or cited literature on other institutional data.

3 Technical Area #1

3.1 Development of Hypoimmunogenic iPSCs (HIP-iPSCs)

3.1.1 HIP-iPSC Generation

In preliminary studies aimed at enabling the production of allogeneic human cells capable of immune evasion, we used human iPSCs obtained from Reprocell (Yokohama, Japan) that had been genetically modified via CRISPR/Cas9 to knock out *B2M* and *CIITA*, thereby abolishing surface expression of HLA class I and II (**Fig. S3A**). To further protect against clearance by NK cells and macrophages, we introduced a lentiviral vector encoding CD47, an innate immune checkpoint ligand that binds SIRPα on effector cells and delivers a "don't eat me" signal [76–78]. $CD47^+$ clones were enriched by flow cytometry and clonally expanded to generate hypoimmunogenic iPSC (HIP-iPSC) lines. Molecular analyses confirmed successful editing and immune-modulatory transgene expression. qPCR revealed robust CD47 expression in HIP-iPSCs, while pluripotency markers *OCT4*, *NANOG*, and *SOX2* remained unchanged relative to controls (**Fig. S3B**). Flow cytometry showed a ~3.5-fold increase in CD47 surface expression in HIP-iPSCs compared to wild-type levels, exceeding thresholds reported to suppress innate cytotoxicity [77](**Fig. S3C**). These results demonstrate the generation of human HIP-iPSCs with retained pluripotency and multi-layered immune shielding.

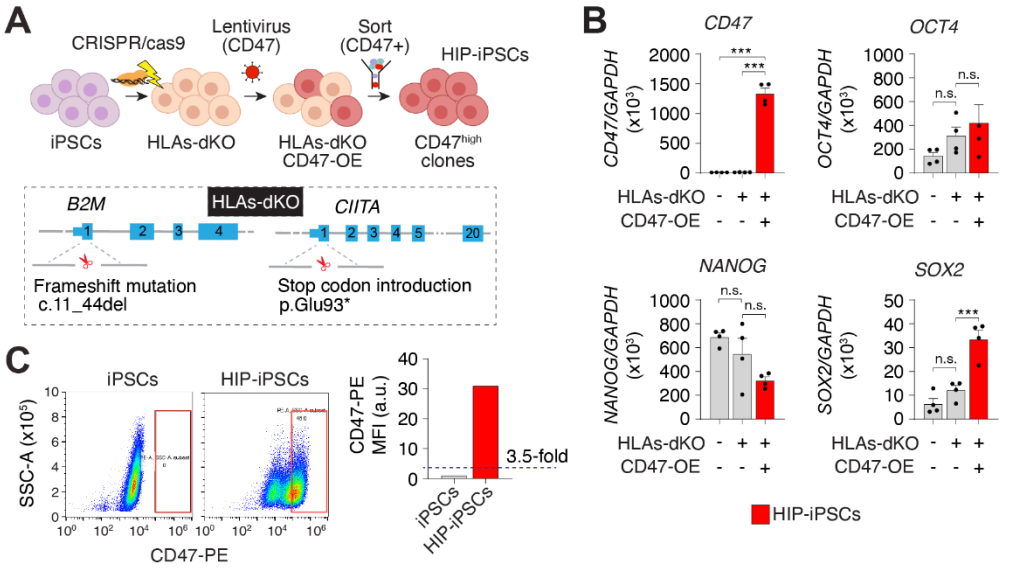

Fig. S3: Generation of hypoimmunogenic iPSCs (HIP-iPSCs) by HLA class I/II double knockout and CD47 overexpression. (**A**) Human iPSCs were modified via CRISPR/Cas9 to delete *B2M* and *CIITA*, abolishing HLA class I and II expression, and then transduced with a lentiviral vector encoding CD47. CD47⁺ cells were enriched and clonally expanded. (**B**) qPCR confirmed strong *CD47* overexpression and maintained expression of pluripotency markers *OCT4, NANOG*, and *SOX2*. (**C**) Flow cytometry revealed a ~30-fold increase in CD47 surface levels compared to wild-type, exceeding the ~3.5-fold threshold.

3.1.2 HIP-iPSC Differentiation into Vascular Lineages with Preserved Immune Evasion

We next assessed whether HIP-iPSCs could be directed into therapeutically relevant lineages without loss of immune protection. Using a non-integrative, chemically modified mRNA (modRNA)–based protocol, we induced HIP-iPSCs toward endothelial and mural fates by delivering ETV2 and NKX3.1, respectivel[79,80] (**Fig. S4**). Sorted populations expressed canonical lineage markers by qPCR, including *PECAM1*, *CDH5*, and *VWF* in in HIP-induced endothelial cells (HIP-iECs), and *ACTA2*, *TAGLN*, and *CNN1* in HIP-induced mural cells (HIP-iMCs) (**Fig. S4A–B**). Immunofluorescence confirmed protein-level expression of VE-cadherin, CD31, and VWF in HIP-iECs, and α-SMA, SM22, and calponin in HIP-iMCs (**Fig. S4C–D**). Critically, flow cytometry demonstrated complete absence of HLA class I and II surface molecules (HLA-ABC, HLA-DR) in both iECs and iMCs) (**Fig. S4E–F**), confirming the stability of the *B2M*/*CIITA* knockouts post-differentiation. Together, these data show that HIP-iPSCs retain full differentiation competence and give rise to lineage-committed vascular cells with intact immune-evasive features, establishing a viable platform for building multicellular, off-the-shelf constructs from human cells.

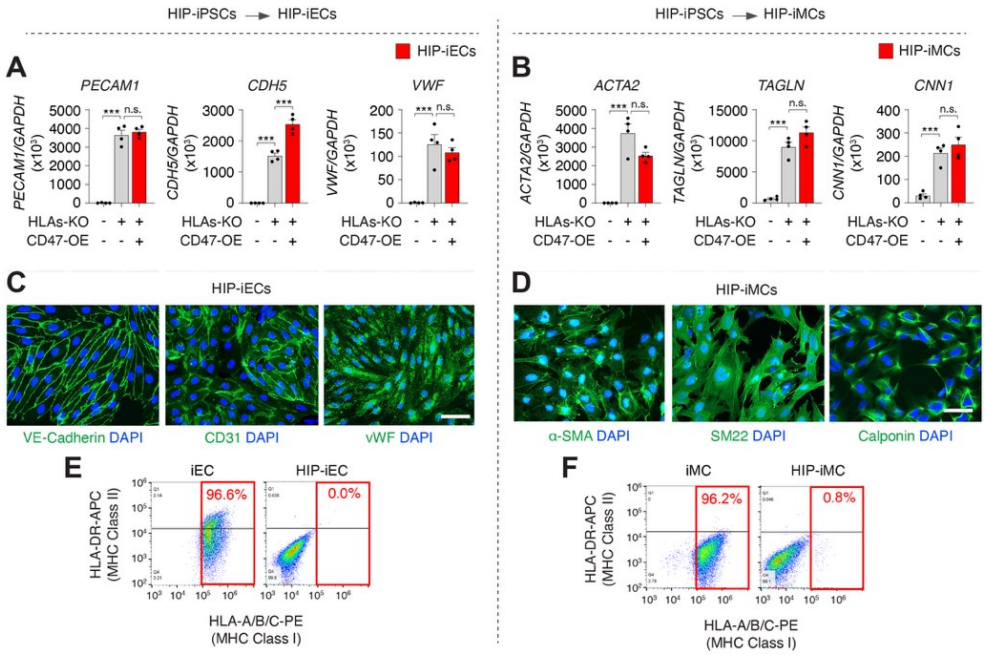

Fig. S4: Differentiation of HIP-iPSCs into hypoimmunogenic vascular cells lacking HLA expression. HIP-iPSCs were directed into endothelial (HIP-iECs) or mural (HIP-iMCs) lineages using modRNA encoding ETV2 or NKX3.1, respectively. (**A–B**) qPCR confirmed expression of endothelial markers (*PECAM1, CDH5, VWF*) in HIP-iECs and mural markers (*ACTA2, TAGLN, CNN1*) in HIP-iMCs. (**C–D**) Immunofluorescence verified protein expression of VE-cadherin, CD31, and VWF in HIP-iECs, and α-SMA, SM22, and calponin in HIP-iMCs. (**E–F**) Flow cytometry confirmed the absence of HLA-ABC (class I) and HLA-DR (class II) on both HIP-iECs and HIP-iMCs, validating successful immune engineering.

3.1.3 HIP-iEC and HIP-iMC Immune Evasion In Vitro and In Vivo

We next tested whether our hypoimmunogenic vascular cells could evade allogeneic immune responses using in vitro and in vivo assays (**Fig. S5**). To assess T cell responses, we adapted a co-culture system in which target cells are pretreated with IFN-γ to induce MHC expression, then incubated with CFSE-labeled human T cells (isolated via negative selection from peripheral blood) for 7 days (**Fig. S5A**). T cell proliferation, a surrogate of activation, was measured by CFSE dilution via flow cytometry. As expected, wild-type iECs co-cultured with allogeneic T cells exhibited signs of immune attack, including T cell clustering and destruction of the endothelial monolayer (**Fig. S5B**). In contrast, HIP-iECs maintained an intact morphology and showed no visible immune-mediated damage. Flow cytometry confirmed a dramatic reduction in $CD3^+$ T cell proliferation in HIP-iEC co-cultures (2%) versus control iECs (24%) (**Fig. S5C**), with similar results observed for HIP-iMCs. Quantification showed significant protection from $CD3^+$, $CD4^+$, and $CD8^+$ T cell responses in both HIP-iECs and HIP-iMCs (**Fig. S5D**). HLA double knockout

(HLA-dKO) cells conferred only partial protection, whereas HIP cells with CD47 overexpression showed near-complete T cell evasion.

To evaluate susceptibility to innate immune attack, we used complementary in vitro and in vivo NK cell assays. In vitro, vascular cells were pretreated with IFN-γ and co-cultured with allogeneic NK cells for 20 hours (**Fig. S5E**). Target cell survival was measured by flow cytometry, and NK cell activation was quantified via CD107a surface expression. HIP-iMCs showed enhanced survival and reduced NK degranulation compared to HLA-dKO controls, indicating improved innate immune evasion (**Fig. S5F–G**). HIP-iECs showed variable protection across donors (not shown), suggesting that additional engineering may be needed to reinforce endothelial resilience to NK cytotoxicity. In vivo, we transplanted luciferase-expressing HIP-iPSCs or HLA-dKO iPSCs into nude mice (which lack T cells but retain NK function) and tracked persistence via longitudinal imaging. HIP-iPSCs displayed significantly greater survival than HLA-dKO iPSCs (~2-fold at day 6), indicating partial evasion of NK-mediated clearance in vivo (**Fig. S5H**). These data support the use of our engineered HIP platform to generate both undifferentiated and differentiated human cells with multi-axis immune evasion.

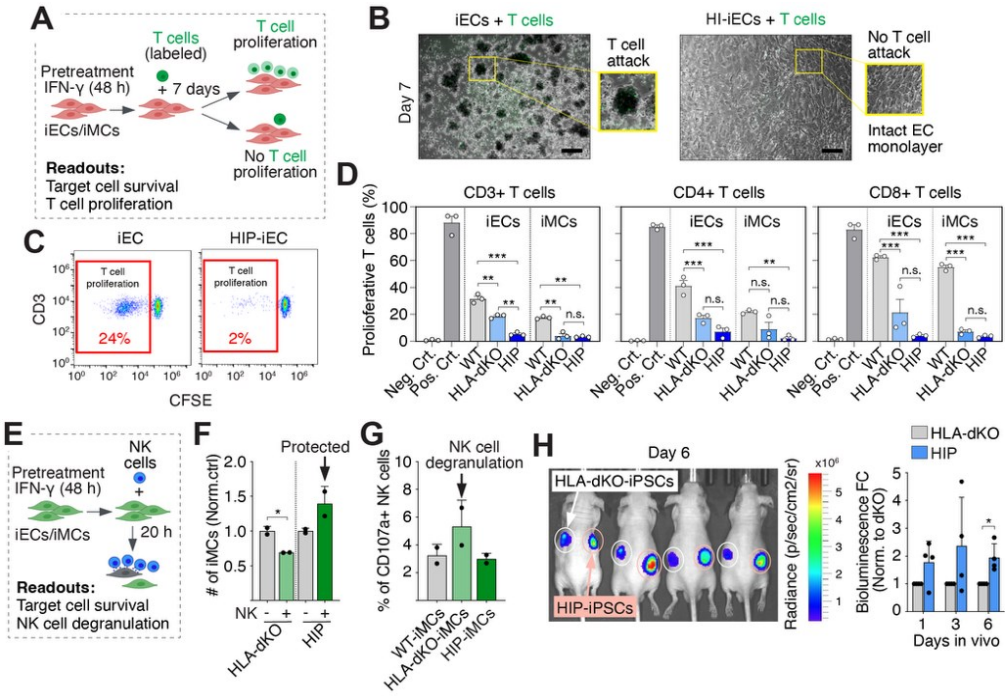

Fig. S5: Evaluation of immune evasion by hypoimmunogenic vascular cells. (**A**) Schematic of T cell proliferation assay: target iECs/iMCs were pre-treated with IFN-γ and co-cultured with CFSE-labeled human T cells from allogeneic donors for 7 days. (**B**) Phase contrast images show T cell clustering and monolayer disruption in control iECs (left), but intact monolayers in HIP-iECs (right). Scale bar, 100 µm. (**C**) Representative FACS plots show reduced CFSE dilution in HIP-iECs, indicating diminished T cell proliferation. (**D**) Quantification of proliferating $CD3^+$, $CD4^+$, and $CD8^+$ T cells in co-culture with iECs, iMCs, $HLA^{-/-}$ cells, or HIP-iECs/HIP-iMCs; negative control: T cells alone, positive control: anti-CD3/CD28 beads. (**E**) Schematic of NK cell co-culture assay. iECs/iMCs were pretreated with IFN-γ and exposed to allogeneic human NK cells for 20 hours. (**F**) Quantification of surviving iMCs by flow cytometry. (**G**) Quantification of $CD107a^+$ NK cells following co-culture with WT, HLA-dKO, or HIP-iMCs. (**H**) In vivo NK clearance assay. Luciferase-labeled HIP-iPSCs and HLA-dKO iPSCs were implanted into nude mice; bioluminescence imaging over 6 days revealed improved persistence of HIP-iPSCs relative to HLA-dKO controls.

3.2 Bioreactor Generated Cardiomyocytes

We have developed protocols based on suspension culture of embryoid body (EB) for the differentiation of iPSCs into ventricular cardiomyocytes (ivCM), which yield the highest reported efficiency of cardiomyocyte production and demonstrate superior functional performance compared to conventional monolayer approaches[81]. In this method, iPSCs are first aggregated into EBs in suspension culture, followed by stage-specific modulation of Wnt signaling: initial activation with the small molecule CHIR99021, followed by inhibition using IWR1 to promote cardiac lineage specification (**Fig. S6A**). The 3D differentiation was carried out in a well-controlled DASGIP® Parallel Bioreactor System, as described in our published protocol. To evaluate differences in cardiomyocyte yield and purity of our 3D and standard 2D protocol, we employed wild-type male hiPSCs and applied a 15-day differentiation protocol modulating Wnt/β-catenin signaling via CHIR-99021 and IWR-1 (**Fig. S6A**). Following harvest on day 15, cardiomyocyte identity and purity were assessed by flow cytometry for the cardiac marker TNNT2 (**Fig. S6B**). Our 3D bioreactor differentiation produced significantly high cell yields (~121 million cells/100 ml) and improved cardiomyocyte purity (>90% TNNT2+) (**Fig. S6C**), demonstrating enhanced scalability and efficiency of the suspension-based approach.

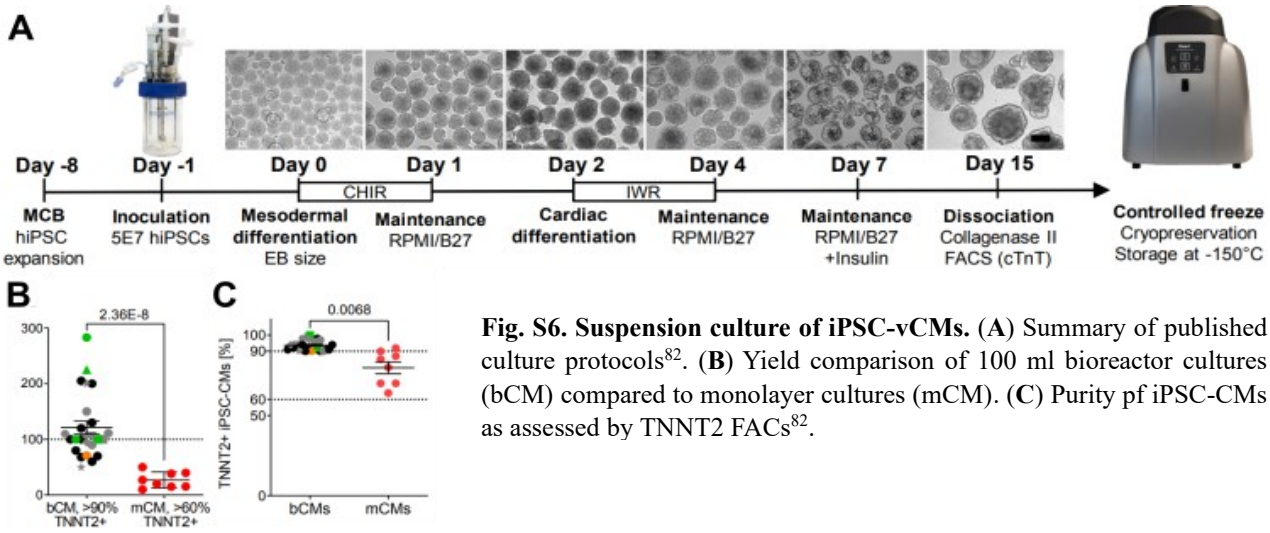

Fig. S6. Suspension culture of iPSC-vCMs. (**A**) Summary of published culture protocols[82]. (**B**) Yield comparison of 100 ml bioreactor cultures (bCM) compared to monolayer cultures (mCM). (**C**) Purity pf iPSC-CMs as assessed by TNNT2 FACs[82].

3.3 QA/QC with Microphysiological Systems (MPS)

3.3.1 *Cell Architecture and Myofibrillogenesis*

As described in our previous publications [81,82], we will perform structural phenotyping by measuring features such as cell shape, sarcomeric length, sarcomere packing density (SPD), orientational order parameter (OOP), sarcomeric OOP, non-sarcomeric OOP, Z-disks relative presence and α-actinin coverage,[81,82]. These metrics are important, reflecting the ability of the cells to remodel relative to extracellular boundary conditions.

3.3.2 Metabolism

In our prior studies, we have shown how metabolic profiling is crucial to evaluate myocytes identity [82,83]. Thus, we will perform metabolic profiling of the myocytes by measuring oxygen consumption rate (OCR) in monolayers of the cells with the Seahorse assay[82,83].

3.3.3 Electrophysiological Assessment

For sinoatrial nodal cells (SANCs), atrioventricular nodal cells (AVNCs), and His-Purkinje cells (HPCs) we will perform an optical electrophysiologic assessment. This will be performed using induced ChR2-GFP-P2A-Archon1, in combination with a high-speed/content imaging platform (Vala biosciences) to confirm spontaneous beating rates and typical action potential morphology. This includes characteristics such as increased L-type Ca2+ currents in AVNCs, spontaneous beating rates of >60 bpm in SANCs, in addition to unique action potential morphologies for both SANCs and HPCs. To quantify conduction velocities of HPCs, we will use MPS on micro-molded gelatin substrates[84] to induce cellular alignment in combination with high-speed optical mapping.

3.3.4 *Evaluation of Excitation-Contraction Coupling*

As previously shown in our publications [83,85], we will build muscular thin films (MTFs) as engineered laminar myocardium to measure diastolic tension, peak systolic tension, and rate dependent contractile forces[86]. For electrophysiological function, we will conduct optical mapping of calcium or action potential wavefront propagation with calcium and voltage-sensitive dyes[86].

3.3.5 *Functional Validation of Vascular Cells*

Functional validation of iECs will be performed through standardized in vitro assays. Capillary-like network formation on a Matrigel substrate will be assessed (target of ~10 branches/mm²). NO production will be measured by flow cytometry upon exposure to DAF-FM (target of ~5-fold increase 24 hours after exposure). Regulation of leukocyte adhesion will be tested upon exposure to inflammatory cytokine (TNF-α) (target of ~20-fold increase 5 hours after exposure). Finally, the shear stress response and ability to align under flow conditions will be assessed. To validate the functional properties of the iPSC-derived iMCs in vitro, intracellular Ca2+ flux will be measured through vasoconstriction assays, and collagen gel contraction in response to stimulation with vasoconstrictive drugs will be measured.

3.3.6 *Integrated Metrics*

Previously we have used an integrated quantitative metric based on the Sheehy rating index (SRI) in conjunction with machine-learning algorithms, as a quality control standard for monitoring cardiac differentiation protocols87, and to perform structural phenotyping of cardiomyocytes81. This model utilizes a modified form of the Hellinger distance as a statistical measure to evaluate similarities in phenotypic characteristics. This quality-assessment rubric is assessed using multiparametric metrics that capture structural, functional, genetic, and metabolic features. Key structural metrics include sarcomere and myofibril organization, typically quantified by orientational order parameters (OOP), sarcomere length, and packing density, all indicative of tissue anisotropy and cellular maturity.

4 Technical Area #2

4.1 Overview and Expertise of Landmark Bio

Landmark Bio, part of Artis BioSolutions, is a leading provider of comprehensive solutions for cell and gene therapies, RNA medicines, and other advanced therapies. Leveraging enhanced capabilities, strategic alignment, and commercial expertise, Landmark Bio supports life sciences innovators across the full spectrum of therapeutic development.

Originally established through a unique partnership among Harvard University, Massachusetts Institute of Technology (MIT), FUJIFILM Diosynth Biotechnologies (FDB), Cytiva, and Alexandria Real Estate Equities, Inc., Landmark Bio was designed to bridge the gap between groundbreaking research and scalable, high-quality biomanufacturing.

Based in Watertown, MA, Landmark Bio provides end-to-end cell/gene therapy product and process development, biomanufacturing capabilities, and consulting services for life sciences innovators working on novel modalities such as cell, gene, and RNA medicines, and develops innovative manufacturing technologies to enable the advancement of novel therapies. Landmark's services include:

- **Consulting on product development roadmaps:** Including therapeutic discovery research, product design, process design, quality by design strategy, product quality profile development, pre-clinical studies, etc.
- **Development of IND-enabling and launch-capable processes:** Analytical methods, formulations, and robust manufacturing processes.
- **Manufacture of preclinical and clinical supply:** GMP manufacturing for early and late-stage clinical programs.
- **Analytical characterization and process optimization:** Advanced analytics to ensure product quality and consistency.
- **Technology transfer:** Efficient and scalable transfer of manufacturing processes.
- **CMC development and regulatory consulting:** Guidance from early discovery through development and commercialization.

Landmark Bio is uniquely positioned to accelerate the development of advanced therapies. Their combined expertise enables us to support life sciences innovators through every stage of product development, from early research to clinical and commercial manufacturing. They

embrace collaboration opportunities that might be viewed as too early, too risky, too small, or too challenging for typical CDMOs. Recognizing that translation from bench to clinic is on the critical path of therapeutic development, Landmark Bio is dedicated to helping innovators bring life-changing therapies to patients faster. Their team consists of CMC experts with decades of experience in biologics and advanced therapy development. Landmark strives to deliver exceptional services and solutions best for their clients.

5 Technical Area #3

5.1 Printing Platform Development for Heart Parts

The Parker group has developed multiple additive manufacturing platforms and strategies to build heart parts and full heart models. These fabrication strategies rely on combinations of synthetic and natural polymers that provide focal adhesion sites for different cardiac cell types. Different additive manufacturing platforms developed by Parker's group over the past decade have been used to fabricate various cardiac components, including cellularized in vitro ventricle models, acellular heart valve implants, and acellular vascular grafts.

In our previous work [88], we developed a manufacturing platform, rotary jet spinning (RJS), for the rapid and automated fabrication of biomimetic semilunar heart valve scaffolds (**Fig. S7**). Compared with electrospinning, RJS does not rely on an electrostatic field to drive fiber formation, which allows it to utilize a broader range of materials with higher production rate, including those with low dielectric properties or sensitive degradation conditions such as proteins. Utilizing this technique, we engineered fibrous scaffolds with tunable composition, multiscale architecture, and mechanical properties designed to replicate those of the native leaflet fibrosa. We demonstrated precise control over scaffold parameters and provided initial evidence of their biocompatibility and functional performance in vitro. Valves were minimally-invasively deployed via transapical access to the pulmonary valve position in an ovine model and shown to be functional for 15 h.

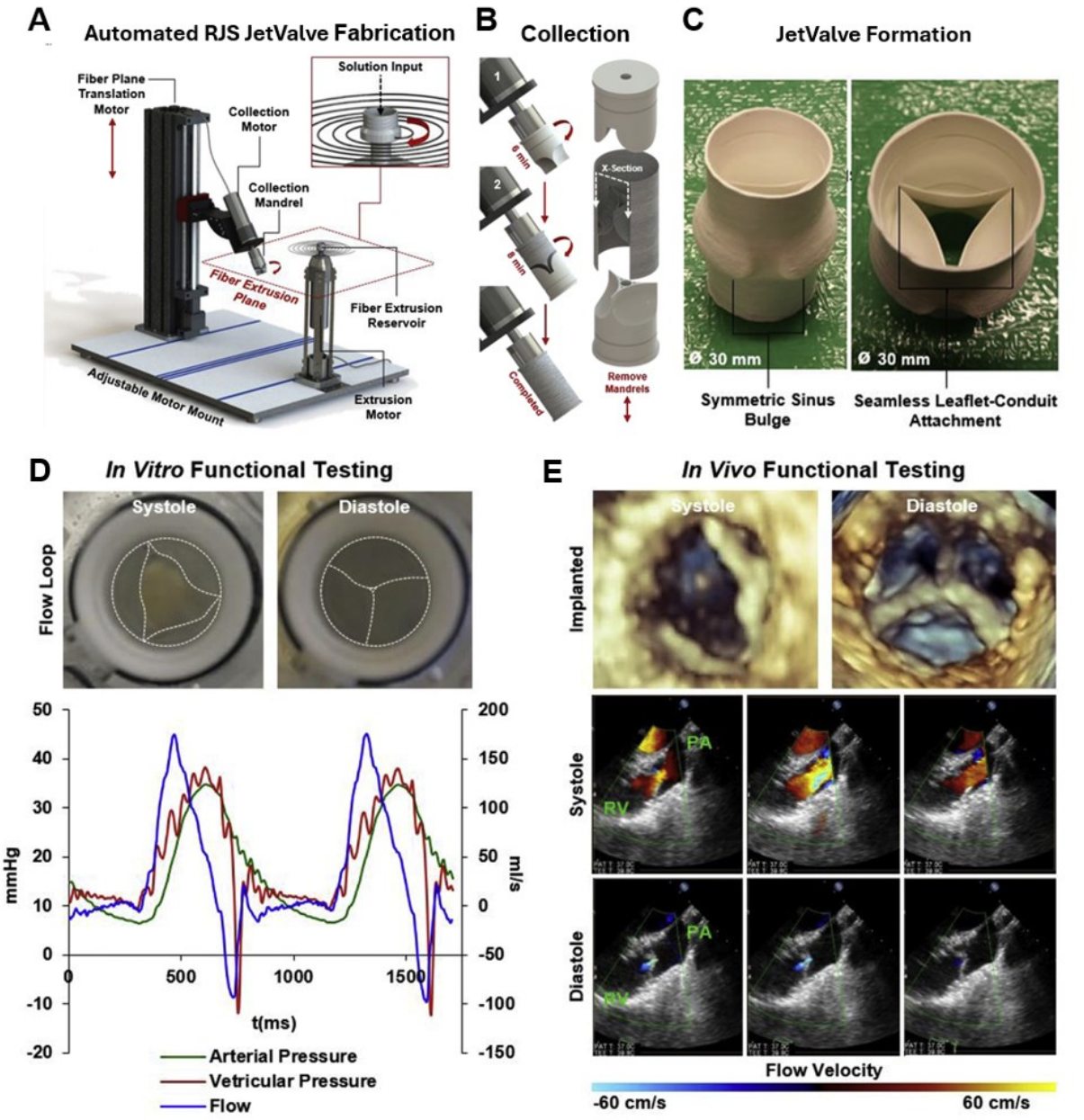

Fig. S7. Rotary jet spinning of cardiac valves. (A) To form ECM mimicking fibers, rotary jet spinning utilizes a high-speed rotational motor to extrude a polymer solution from a reservoir radially into long jets. The jets form fibers from the polymers used as the solute. **(B)** Fibers are collected in the fiber extrusion plane onto a customizable mandrel, in this case a trileaflet valve. **(C)** The resulting scaffolds can form complex geometries on the centimeter scale but maintain nanofiber base units. Adapted from Capulli et al.[88] **(D)** Top: digital photographs from arterial view of mounted JetValves during systole and diastole at 48 h (dotted lines highlight the JetValve leaflet and conduit edges). Bottom: flow through the JetValve reached ~175 ml/s during peak systole with complete valve closure during diastole (~30% regurgitant fraction, ~10 mmHg transvalvular pressure). **(E)** Top: distal three-dimensional echocardiography revealed complete leaflet opening and closing during systole and diastole respectively at 15 h in and ovine model. Bottom: Doppler imaging showed unrestricted blood flow through the JetValve leaflets during systole and complete closure with minor regurgitation fraction during diastole (RV: right ventricle, PA: pulmonary artery).

Next, we developed pull spinning to fabricate nanofibrous scaffolds for tissue engineered human ventricle models (**Fig. S8**) [89]. These scaffolds are designed to support the formation of anisotropic myocardial tissue with native-like architecture and enable chamber-level contractile function.

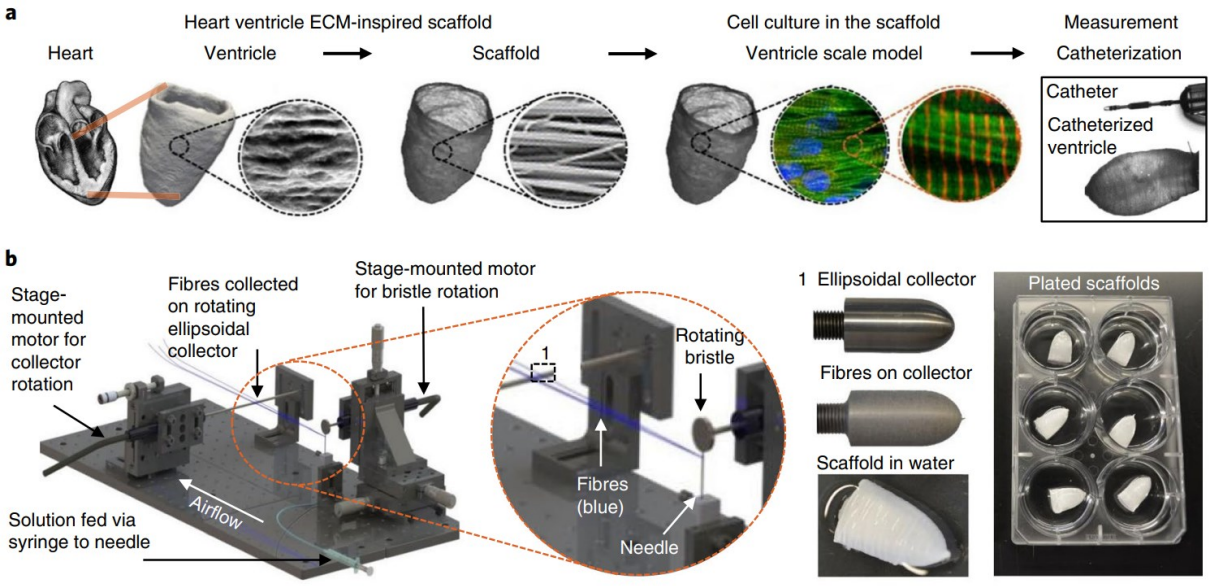

Fig. S8. Pull spinning of cardiac ventricles. (a) Native ventricles enable function through a combination of cardiac muscle and structural ECM. Seeding ECM-mimicking aligned nanofibers with cardiomyocytes created organized muscle structures, allowing for the recreation of cardiac function. **(b)** The aligned nanofiber ventricles were fabricated using pull spinning, a technique that relies on a rotating bristle that pulls a polymer solution, throwing fibrous jets towards a collection mandrel. Adapted from Macqueen et al.[89]

More recently, we continued to evolve fabrication platforms and developed the Focused Rotary Jet Spinning (FRJS) system, an on-demand, high efficiency method for the fabrication of customizable, biomimetic fiber scaffolds[90]. FRJS harnesses centrifugal forces in combination with focused airflow to produce nanofibers and precisely guide their deposition onto customizable mandrels. This approach enables the rapid fabrication of micro- and nanofibrous heart valve scaffolds in under 10 minutes with anatomically relevant valve architectures (**Fig. S9**). We confirmed the valve's ability to regulate cardiac flow both in vitro and in vivo with ovine model.

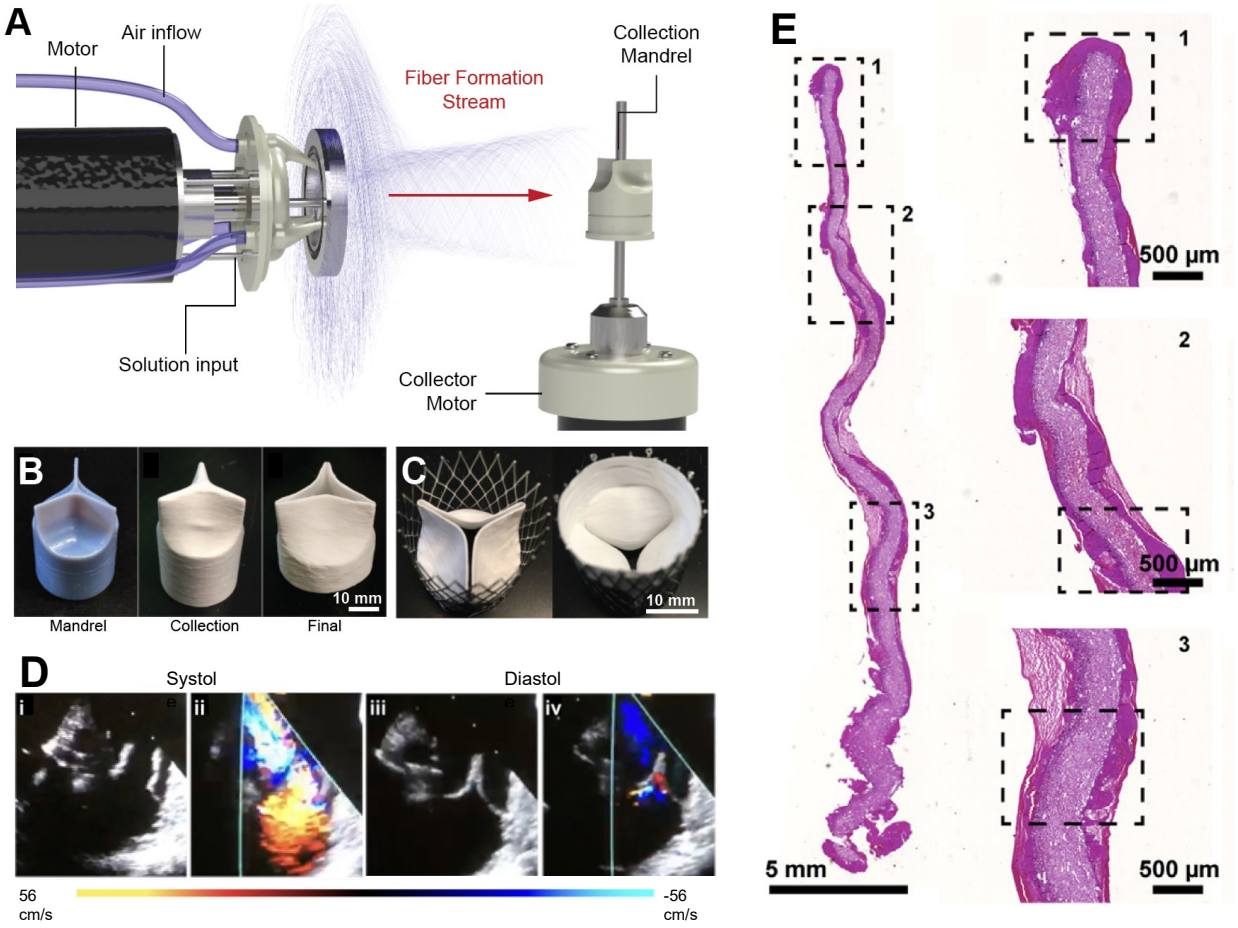

Fig. S9. FRJS of cardiac valves. (A) Utilizing FRJS with a customizable valve shape collection mandrel, yields **(B)** valvular constructs that can be slightly modified to form a full valve replacement. **(C)** These implants can be sutured into stents to facilitate a minimally invasive transcatheter delivery. Adapted from Motta, Peters, Chantre et al.[90] **(D)** Echocardiographic assessment of valve functionality in vivo showing correct leaflet motion and performance during systole (Di and Dii) and diastole (Diii and Div). **(E)** Post-mortem macroscopical and histological evaluation of implanted FibraValve. H&E staining shows retained leaflet morphology after 1 h in ovine model.

We leveraged the FRJS system for the fabrication of ventricle models with controlled tissue alignment[91]. Notably, constructs with helical fiber alignment exhibit more uniform deformation patterns, enhanced apical shortening, and improved ejection fractions relative to those with circumferential alignment (**Fig. S10**).

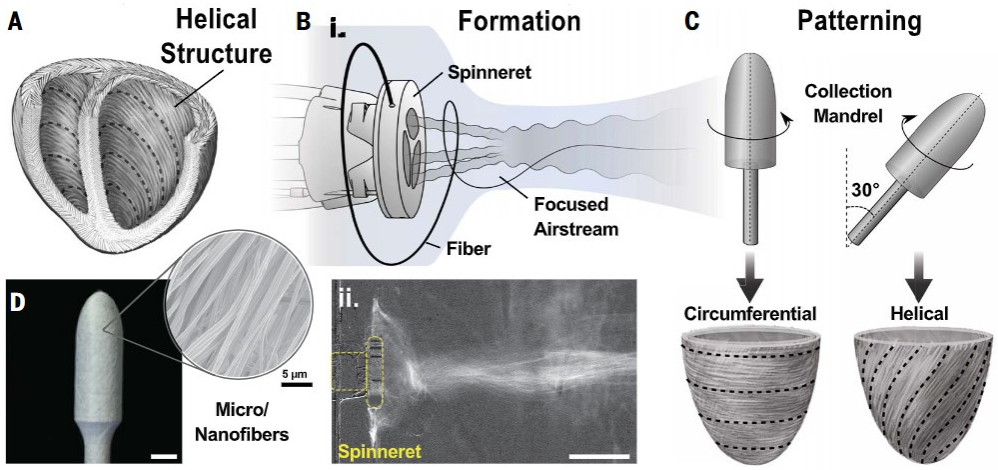

Fig. S10. FRJS of helical cardiac ventricles. (A) Native myocardial tissue is wrapped helically with the alignment transitioning transmurally from a left- to right-handed helix. **(B)** FRJS relies on a high speed rotational motor that expels a polymer solution through lateral orifices. The polymer solution extends radially into solution jets that form polymeric fibers. (ii) These fibers are then directed towards a downstream collector by a focused airstream. **(C)** Adjusting the collector angle in relation to the airstream can alter the collection of the fibers, allowing for control over fiber alignment direction. **(D)** The resulting product is an aligned micro/nanofibrous scaffold in the shape of the collection mandrel (ventricle shape). Scale bars: (Bii) 5 cm and (D) 5 mm. Adapted from Chang, Liu, Zimmerman et al.[91]

Recently, Parker's group has improved its methods for manufacturing an avascular ventricular chamber. Using FRJS to spin fibrous scaffolds doped with sacrificial materials that are eliminated before cell seeding, we built ventricular scaffolds, seeded them with neonatal rat ventricular myocytes, and measured pumping efficiency. In a Langendorff-like setup, we quantified the ejection fraction with particle image velocimetry (PIV) and obtained the deformation map of the ventricle models (**Fig. S11**). The representative ventricle in **Fig. S11** showed an ejection fraction of 16.2%, a significant improvement over our previously reported data[89,91,92]. We hypothesize that the elimination of the sacrificial fibers is resulting in better cell infiltration of the scaffold. We will continue to develop manufacturing methods to replicate the mechanically advantageous architecture of the human ventricle.

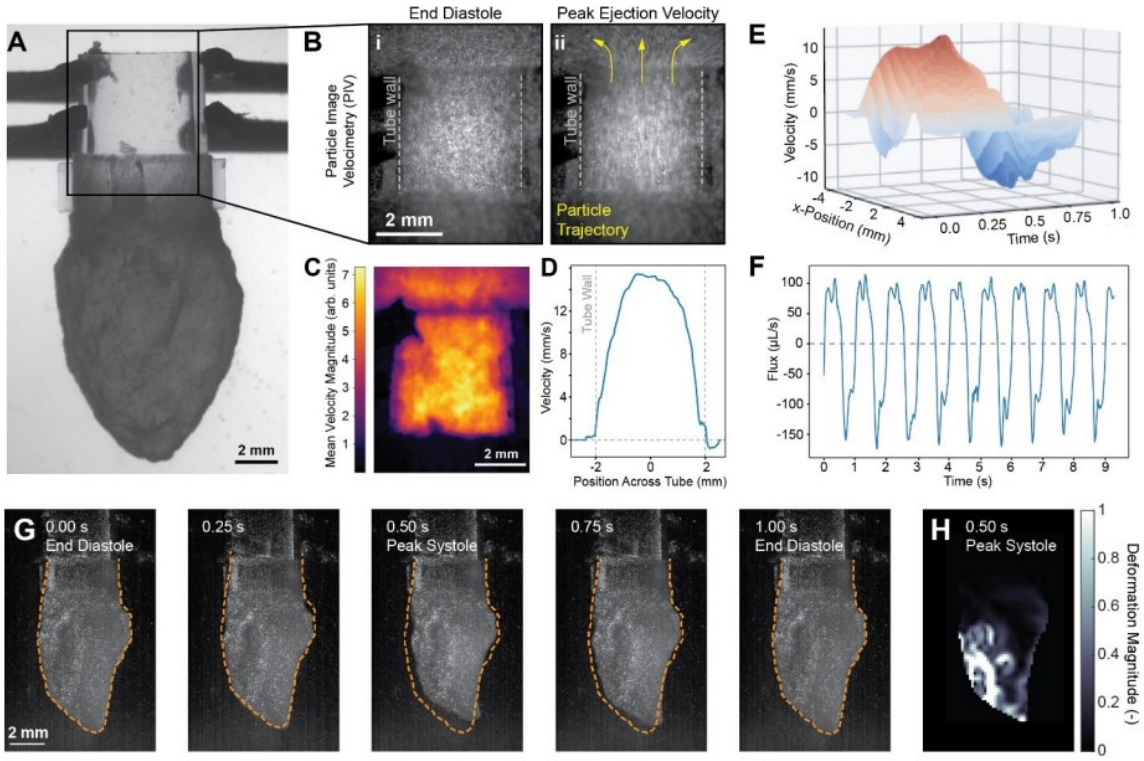

Fig. S11. Unpublished Data: Pumping performance of tissue engineered avascular ventricle. (**A**) A Langendorff-like horizontal setup was used to measure the pumping function of the tissue-engineered ventricle (seeded with NRVM) connected to transparent tubing. (**B**) Representative frames from a particle image velocimetry (PIV) video showing fluorescent bead motion at (i) end diastole and (ii) peak ejection velocity under 1 Hz field stimulation. (**C**) Mean velocity magnitude map derived from the PIV video in (B), highlighting spatial distribution of flow. (**D**) Velocity profile across ventricle annulus. (**E**) Spatiotemporal velocity profile extracted across the tube diameter over one cardiac cycle. (**F**) Flux as a function of time calculated from PIV data. Integration over nine full cardiac cycles yielded an average stroke volume corresponding to a 16.2% ejection fraction in the representative sample. (**G**) Time-lapse images showing ventricle shape changes during contraction. The ventricles exhibit apical shortening and deformation. (**H**) Spatial distribution of deformation magnitude at peak systole, quantified as the Frobenius norm of the Green-Lagrange strain tensor. Strain was computed via digital image correlation applied to the time-lapse sequence in (G), using the end-diastolic frame as the reference configuration.

Additionally, we have recently submitted a manuscript using FRJS to create hierarchical vascular structures that replicate native vessel architecture from the centi- to nanoscale (**Fig. S12**). We fabricated acellular vascular grafts, in less than a minute, that replicated the endothelial cell microenvironment, maintained sub millimeter lumen diameters, all within the centimeter-scale length of the scaffold. The acellular grafts were surgically placed as femoral conduits in rats for approximately one month. The patency of the lumen was maintained, cellular engraftment was observed, and the blood flow, hemoglobin content, and oxygenation of the distal tissues indicated that the graft was successful. Importantly, this illustrates that FRJS additive manufacturing method is capable of building vertically-integrated, hierarchical cardiovascular tissues.

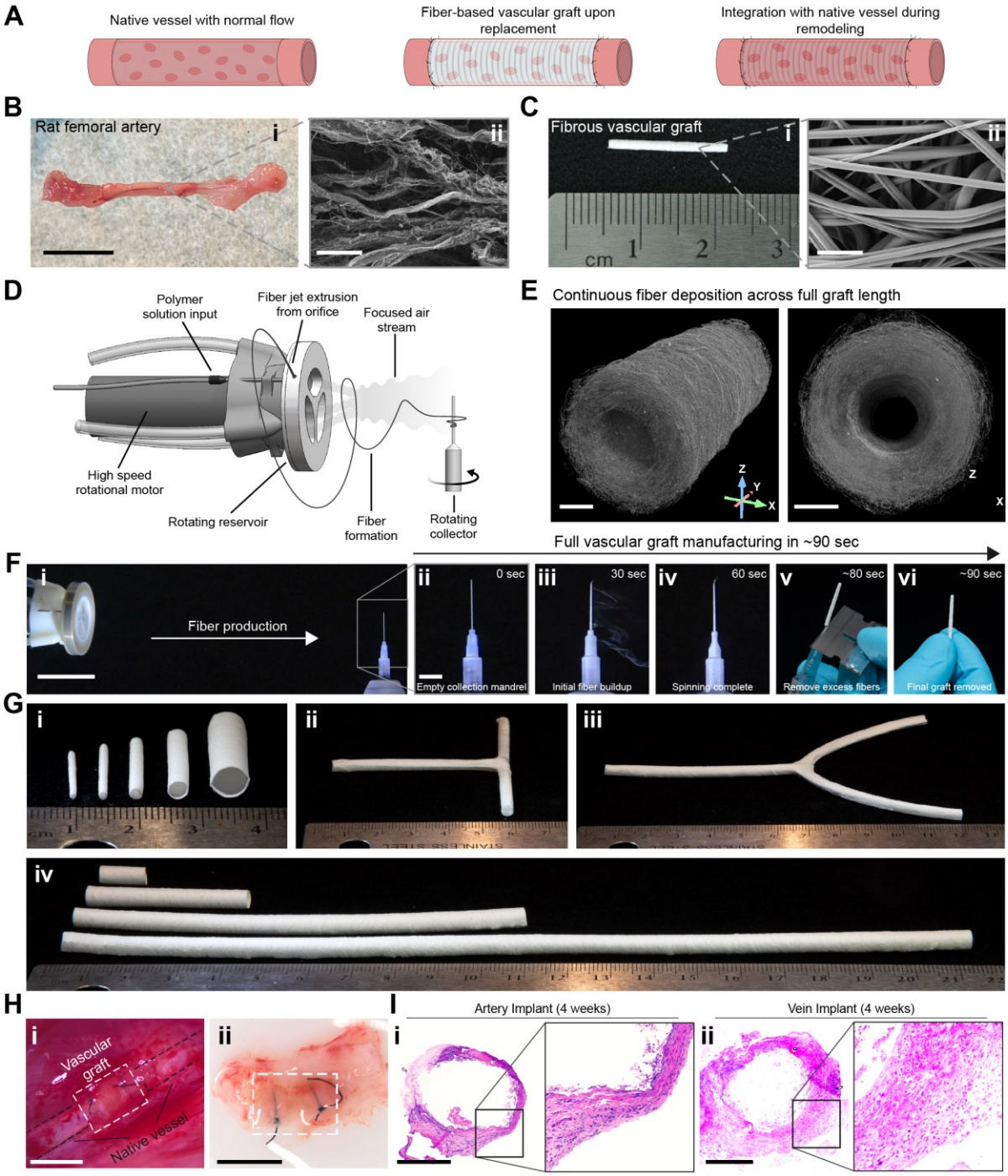

Fig. S12. FRJS of vascular grafts. (A) Inspired by (i) native vasculature's (ii) nano- and microstructural contributions of native ECM, **(B)** we used FRJS to produce hierarchical vascular structures that mimic the native vessel on the (i) centiscale and (ii) microscale. **(C)** The vascular grafts were produced using FRJS. **(D)** Micro computed tomography shows consistent nano- and microfiber deposition across the full wall thickness with a consistent inner lumen diameter present throughout the full graft. **(E)** The vascular grafts are customizable on the centiscale, with control over (i) inner diameter, (ii-iii) vessel branching and curves, and (iv) vessel length. Scale bars: (Ai) 1 cm, (Aii) 5 µm, (Bii) 5 µm, and (D) 250 µm. **(H)** Vascular grafts were (i) implanted in rat femoral vasculature and (ii) explanted at 4 weeks. **(I)** H&E staining shows full cell infiltration in both (i) arterial and (ii) venous implants.

Alternatively, the fiber infused gel (FIG) printing technology was developed to enable the 3D printing of organ-scale scaffolds that recapitulate both intra- and intercellular architecture of the heart (**Fig. S13**)[92]. During extrusion, shear forces align the embedded fibers (produced using FRJS), generating microscale structural cues that guide the self-organization of human cardiomyocytes into anisotropic muscular tissues in vitro. The resulting 3D printed ventricular model demonstrated biomimetic anisotropic behavior and contractile function.

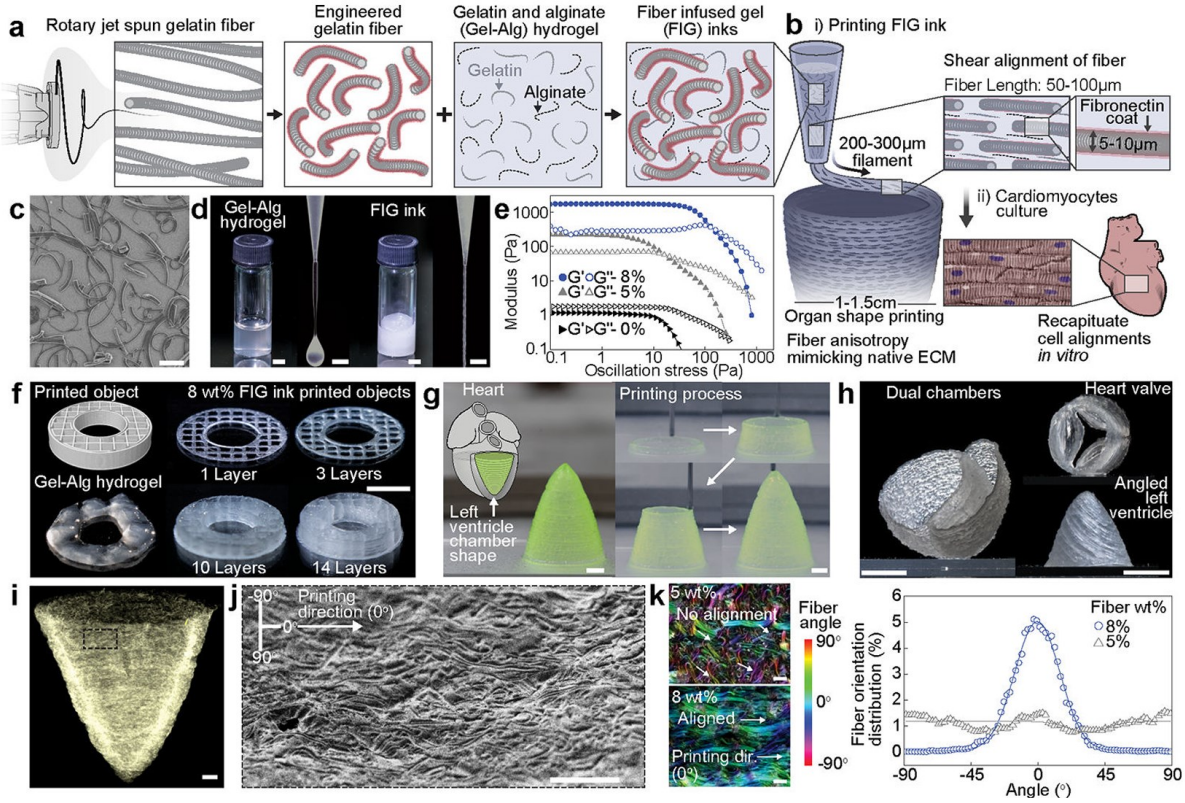

Fig. S13. Fiber infused gel (FIG) printing of cardiac ventricles. (a) In FIG printing, short nanofiber strands are incorporated into a hydrogel ink. **(b)** The FIG ink is then extrusion printed with the shear forces of the print head, aligning the fiber strands in the ink. The fiber strands provide structural cues at length scales below the resolution of the print head. **(c-e)** Tuning the length and concentration of fibers in the hydrogel ink yields different viscoelastic properties, **(f)** allowing for the FIG inks to be printed in larger structures without reliance on a support bath. **(g-h)** This allows for the printed of multiple cardiac components, including (dual) ventricles and valves. **(i-j)** Micro computed tomography and scanning electron microscopy show that the alignment of the short nanofiber stands inside the FIG inks match the printing direction. **(k)** This was quantified at different concentrations, suggesting that sufficient fiber content (8% fiber wt) can instill alignment at length scales familiar to the cellular microenvironment, potentiating cellular alignment. Scale bars: (C) 100 μm, (D) 2 mm, (F) 1 cm, (G) 2 mm, (H) 5 mm, (I) 1 mm, (J) 200 μm, and (K) 100 μm. From Choi et al.[92]

5.2 Process Monitoring of GLP FRJS

To assure quality of scaffold fabrication, fiber production and collection should be consistent and uninterrupted in a controlled environment. Due to FRJS' reliance on solvent evaporation for fiber formation, environmental factors such as temperature and humidity are critically important. **Table S2** outlines environmental factors and suggested tolerances to maintain consistent fabrication outcomes. Additionally, **Table S2** outlines control ranges for FRJS' rotational motor and for the focused air stream directing fibers towards the collection mandrel. Lastly, the table specifies the inks' polymeric quality inputs as the basis of the scaffolds produced.

Design Specification	Process Control Modality	Anticipated Control Range
Temperature	Digital thermocouple	23º ± 1ºC
Relative Humidity	Nitrogen gas infusion	< 5% RH
Airborne particle count	HEPA filtration system	< 100 ppm
Polymer solution viscosity	Rheometer	50 – 300 MPa*s
Solution infusion rate	Automated syringe pump	0.1 – 20 mL/min
Solvent vapor pressure	Photo ionization gas monitor	< 20 ppm
Rotational reservoir speed	Motor feedback controller	10,000 - 80,000 RPM
Rotational fiber collector speed	Motor feedback controller	500 - 10,000 RPM
Fiber deposition rate	Laser distance meter	10 – 35 µm/min
Target deposition distance	Robotic arm feedback controller	20 ± 1 cm
Polymer chain length and distribution	HPLC (High performance liquid chromatography) or GPC (Gel Permeation Chromatography	Specific regarding polymer types

Table S2. GLP FRJS Design Specifications.

5.3 Machine Learning Directed Structural Design

In guiding organ design, Parker's team will develop machine learning models to optimize cardiac structure-function relationships, similar to their previous work[81]. To simulate cardiac contraction, we will use a physics informed neural network as a kinematic model, coupled to a computational fluid-dynamics (CFD) simulation. For kinematic modeling, we will use the Holzapfel and Ogden (Hao) structural model[93] embedded within a physics informed neural network (piNN). Here, the HaO model describes the relative anisotropy and mechanical behavior of a surface, while the piNN is trained to minimize the total potential energy of these surfaces, providing a shape dependent model of cardiac contraction, which can be used as an input for fluid-simulations. For CFD, we will utilize the lattice Boltzmann Method (LBM), which converges to approximate the Navier-Stokes equation[94], and allows simulation of complex geometries[91,95], Altogether, this approach will be used to determine how different design parameters impact key cardiac functions, such as cardiac output/stroke volume[96–99], electrophysiology[100,101], pressure-volume loops[98,99], vascular hemodynamics[96,97,99,102], and ventricle energy dynamics[96,97,99].

5.4 Heart Biofabrication

5.4.1 Atrial Segment

The atrial segment, composed of both the left and right atria, will be fabricated using a combination of FRJS and fiber infused gel (FIG) printing, a technique recently developed in the Parker lab which uses nanofibers embedded in 3D printing inks to induce tissue anisotropy[92]. To create the partially enclosed chambers, fibers will be spun onto sacrificial molds as previously demonstrated[91] **(Fig. 18**). Specific chamber geometries will be based off a combination of raw scans, and machine-learning informed design. During spinning, both SA and AV nodal constructs will be integrated directly in the chamber design (See SA/AV Node Fabrication). To bridge conduction between the two segments, a biomimetic atrioventricular bundle will also be fabricated, descending from the atrial segment inferiorly towards the ventricular segment. During assembly, this will be sutured to the superior extension of the ventricular segment. In addition to SA/AV nodes, a dual chamber pacemaker lead will be attached to the epicardial surface of the right atrium,

serving as a recording device to monitor the transition between in vitro culture and in vivo implantation, as well as mitigation strategy for conduction system failure.

5.4.2 SA/AV Node Fabrication and Integration

Nodal host scaffolds will be manufactured using FIGs 3D printing. This will result in tissues with controlled alignments and geometries, that are surrounded in part on either side by a hydrogel insulating layer, explicitly regulating myocardial connections and source-to-sink relationships[103], while ensuring physiological conduction[104]. Previously, we have achieved a similar result in 2D systems, using a geometrically isolated myocardial tissue to form a spontaneously paced node-like structure (G-Node)[105]. Scaling these geometric cues to 3D tissues, we will form SA/AV nodal mimics, which can be integrated directly within the atrial wall. The SA nodal mimic will be integrated on the epicardial surface of the full heart construct near the superior cavo-atrial junction and attached to the heart with fibrin glue[106]. Care will be taken to ensure the "active" portion of the SA nodal mimic containing differentiated and aligned SANCs is in direct contact with the atrial surface. The AV nodal mimic will be integrated into the floor of the RA prior assembly of the AV valves and will be secured into place near the inflow point for the His-purkinje channels by fibrin glue or sutures. This will combine cellular (SANCs/AVNCs) and structural features[107] to induce decremental conduction velocities, which we will confirm to proceed only through the AV node and the biomimetic atrioventricular conductive bundle.

5.4.3 Ventricular Segment, Vascular and Conduction System Integration

A dual chambered ventricular segment will be fabricated using FRJS spinning. This segment will encompass both the left and right ventricles, as well as the beginning of the respective outflow tracts. Fabrication will preserve the inherent helical and circumferential alignment of the corresponding chambers, as previously demonstrated in a rat scale dual-chambered ventricle model[91] (**Fig. S14**). While spinning these fiber scaffolds, sacrificial channels will be introduced for both the vasculature and for the cardiac conduction system (See Vascularized Tissue Constructs section in main proposal). Ventricular vasculature will include a biomimetic coronary artery, with the proximal end descending from the outflow tract of the aortic valved conduit. This network will extend transmurally throughout the ventricle wall, before ending in a biomimetic coronary sinus, which will be sutured to the right atrium during assembly to facilitate drainage. For the conduction system, sacrificial channels will be created within the interface of the two chambers

(intraventricular septum) and extending circumferentially around the two ventricles. An entrance port will be left on the right atrial side of the septum for seeding of differentiated HPCs and as a location for placement of the SA nodal mimic, extending from the floor of the RA. The combination of the electrical properties of the differentiated HPCs and aligned nanofibers within the sacrificial channels will promote cardiac tissue alignment [89,108] and anisotropic tissue conduction along the longitudinal axis [91,92], improving and will be used to promote the speed of signal propagation.

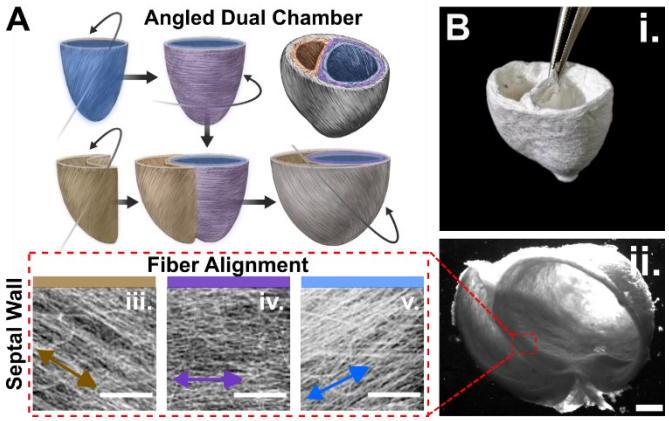

Fig. S14. Multilayered Dual Ventricular Constructs. (**A**) By spinning fibers onto ventricle shape collection mandrels in a multistep fashion, we can create multichambered ventricular constructs with a chiral transition of helical alignments from the endo- to epicardial surfaces. (**B**) The change of helical alignment directions throughout the chamber wall was visualized via scanning electron microscopy. Adapted from [91].

5.4.4 Valved Conduits Fabrication and Integration

We will construct semilunar valved conduits as previously reported[90] to regulate unidirectional blood flow for all four heart valves. Briefly, bioinks will be spun about a tricuspid shaped collection mandrel. Fibers will then be embossed, forming valve leaflets with deep belly curvature, prior to being sutured into their respective annulus. This allows for highly customizable valve components which can be integrated with the heart, ensuring hemodynamic regulation. Cellular components of the valved conduits will include both interstitial and endothelial cellular components. iVICs will be incorporated throughout the leaflet thickness and a monolayer of iEC will be used to endothelialize the exterior of the leaflets.

Prior work has demonstrated that the inclusion of vascular ECs on engineered valves can successfully mitigate thrombosis, promote hemocompatibility, modulate the immune response to the implanted valve, and support VIC homeostasis after in vivo implantation[109–111]. To promote process efficiency, ease of manufacturing, and scalability, cellularized bioprinted valves will be endothelialized with generic iECs that are also utilized in REHEART's engineered vascular and cardiac tissues. Although some transcriptome-level differences have been shown between valvular

and vascular ECs, it is generally thought that the majority of these differences are the result of adaptations to differential hemodynamic environments, and not to fundamental differences in cell type[112]. Notably, during embryonic development of the cardiac valves, valvular endothelial cells (VECs) are derived from the endocardium[113] – further supporting the approach of sharing generic iECs between our engineered cardiac and valvular tissues. Should unexpected challenges arise in maintaining valvular or myocardial function that are attributed to a lack of specific EC subtype, then we will generate iPSC-derived versions of these specialized cell types (*e.g.*, endocardium[114], VECs[115,116]) and include them in our engineered tissues.

Component	Assembly Process
Atria	1. Seed atrial walls via vena cava (right) / pulmonary vein (left), using 3D bolus injection (aCMs) 2. Seed SA and AV nodes via vena cava using 3D bolus injection (SANCs & AVNCs) 3. Seed biomimetic atrio-ventricular bundle via vena cava using 3D bolus injection (HPCs), connect the SA and AV nodes 4. Culture in bioreactor (2-3 weeks)
Ventricle	1. Perfuse vasculature via biomimetic coronary sinus and coronary artery (iECs and iMCs) 2. Perfuse factors promoting *de novo* angiogenesis via biomimetic coronary sinus and coronary artery 3. Perfuse conductive channel via atrio-ventricular opening (HPCs) 4. Seed ventricle walls via right and left atrio-ventricular opening using 3D bolus injection (vCMs) 5. Seed pulmonary and aortic arteries via surface using 3D bolus injection (iECs and iMCs) 6. Culture in bioreactor (2-3 weeks)
Valves	1. Seed valves via surface using 3D bolus injection (iVICs) 2. Seed endothelial monolayer of iEC on the exterior of leaflets 3. Culture in bioreactor (2-3 weeks)
Assembly	1. Suture atrial and ventricular segments together, leaving access to the internal structure via predetermined atrial incisions 2. Suture biomimetic atrial bundle from the atria into the septal wall of the ventricle containing the His bundle-Purkinje fibers, connecting the atrial/ventricular conduction systems 3. Implant valves (2 atrioventricular, 2 outflow tract) via Ross II and Bentall techniques, respectively 4. Thread biomimetic coronary sinus from the endocardial surface into the right atrium, and suture via collar, connecting the atrial/ventricular vasculature 5. Suture proximal end of coronary artery to aortic root to allow for antegrade perfusion 6. Suture closed predetermined atrial incisions 7. Culture in perfused bioreactor (2-3 weeks), monitoring cardiac function and cardiac electrical conduction tracings

Table S3. Bioprinted Heart Assembly.

5.5 Animal Study Plans

To test the function, engraftment, and immune compatibility of the hypoimmune cell types, the heart parts, and full hearts that we are printing, we will perform small and large animal studies, systematically evaluating each cellular and scaffold component. Phase I will employ 68 small animal models, while Phase II will employ 39 large animal models. An overview of the animal study plans can be found in **Table S4**.

Animal Model							Heart Component [Cell Types]					
Phase (Milestone)	Task	Study #	Animal Model	Acuity Animal #	Implant Component	Purpose of Study	Ao / Pulm Valve [iVIC]	Ventricular Patch [iaCM, ivCM]	Vascular Graft [iEC, iMC]	SA & AV Node His-Purkinje Bundle [iSANC, iAVNC, iHPC]	Single Ventricle	Full Heart
Phase I (3.6) Mice	15.2	1	NSG Mouse (Immunodeficient)	Chronic n = 16	Cells Only (Hypoimmune)	Teratoma Assay	2	4	4	6		
		2	NSG Mouse (Immunodeficient)	Chronic n = 4	Cells Only (Hypoimmune)	Teratoma Assay ("+" Control)	1	1	1	1		
	15.3	3	Humanized Mouse	Chronic n = 16	Cells Only (Hypoimmune)	Immune compatibility	2	4	4	6		
		4	Humanized Mouse	Chronic n = 16	Cells Only (Non-hypoimmune)	Immune compatibility ("+" Control)	2	4	4	6		
		5	NSG Mouse (Immunodeficient)	Chronic n = 16	Cells Only (Hypoimmune)	Immune compatibility ("-" Control)	2	4	4	6		
Phase II (3.7) Pigs	21.2	6	Pre-Immune Neonatal Pig (Wild Type)	Acute n = 12	Cellularized Bioinks/Scaffolds (Hypoimmune)	Function / Engraftment / Immune compatibilty	3	3	3	3		
		7		Chronic n = 12			3	3	3	3		
	21.3 to 24.2	8	Pre-Immune Neonatal Pig (Wild Type)	Acute n = 6	Cellularized Bioinks/Scaffolds (Hypoimmune)	Function / Engraftment / Immune compatibilty					3	3
		9		Chronic n = 9							3	6

Table S4. Detailed Animal Study Overview. Small animal models will be used to evaluate each cell in teratoma formation assays and immune compatibility assays. Similarly, in a large animal model, all heart part scaffolds will be evaluated (testing function, engraftment, and immune compatibility) before single ventricle, full heart (heterotopic), and full heart (orthotopic) implants are performed.

In studies 8 and 9, the bioprinted heart will be implanted in pre-immune neonatal pigs and survived for 24 hours (acute) and 4 weeks (chronic). The hearts will first be implanted heterotopically via anastomoses of the biofabricated atria to the recipient atria and the biofabricated valved outflow tracts to the recipient outflow tracts (**Fig. S15**). The engineered heterotopic heart will assist in pumping, gradually taking on more load and maturing.

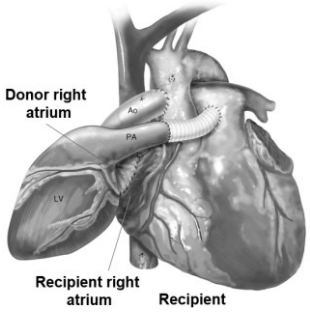

Fig. S15. The Heterotopic Heart Transplant was developed in 1983 by Christiaan Barnard[137,138]. The atria and ventricular outflow tracts are coupled, essentially making the heterotopic transplant a cardiac assist device.

5.6 Teratoma Assay

For teratoma assay testing, all differentiated hypoimmune cell types (aCMs, vCMs, SANCs, AVNCs, HPCs, iECs, iMCs, iVICs) will be subcutaneously injected into the dorsal lateral flank of an immunodeficient mouse[117]. One cell type will be injected into each mouse. Following the survival timeframe, explants will be evaluated using histological analysis to assess the presence or absence of teratoma formation. Undifferentiated hypoimmune parental iPSCs will serve as a positive control, as they are expected to form teratomas.

5.7 Immune Compatibility

For immune compatibility testing, all differentiated cells types derived from a luciferase-labeled hypoimmune iPSC line will be subcutaneously injected into the dorsal lateral flank of a humanized mouse[117,118]. One cell type will be injected into each mouse. As a positive control, humanized mice will be transplanted with differentiated cells derived from a luciferase-labeled parental (non-hypoimmune) iPSC line. It is expected that the positive control will be rejected given the non-hypoimmune cell line, while the hypoimmune cells will engraft and survive. For a negative control group, immunodeficient mice will be transplanted with differentiated cell types derived from the luciferase-labeled hypoimmune iPSC line. It is expected that the negative control will not be rejected given the immunodeficient mouse model. Following injection, all mice will be survived for at least 4 weeks and intravital luciferase signals in the hypoimmune cells transplanted in the humanized mice will be compared to the positive and negative control groups using IVIS to measure graft acceptance and survival. At the end of the study, the grafts will be collected for immunohistochemistry to evaluate immune compatibility. The Melero-Martin group has extensive experience in subcutaneous implantation of vascular networks using a similar approach[119,120].

5.8 Animal Study Metrics and Readouts

For myocardial patch and valve implants, ECHO will be used to evaluate global cardiac and valve function, respectively. For vascular graft implants, ultrasonic doppler will be used to evaluate vessel patency. For conduction system implants, electrocardiography and pacer recordings will be used to evaluate rhythm and presence of arrhythmias. For cellular implants of all heart components, explants will be evaluated using histological analysis to assess

bioink/scaffold immune compatibility and cell engraftment. Single ventricle and full heart implants will be evaluated using all mentioned immunochemical and monitoring modalities. Furthermore, for survival studies, the native heart inflow of the single ventricle and full heart constructs will be restricted via endovascular occlusion of the native atrioventricular valve, facilitating increased venous return through the bioprinted organ. Single ventricle and full heart implants will then undergo conductance catheter evaluation to generate pressure-volume loops to assess graft volume loading and function, allowing for determination of graft preparedness and selection of a balloon inflation level that ensures manageable inflow to the graft. Additionally intraoperative monitoring will be used, including: oxygen saturation (pulse oximetry), core temperature (rectal thermometer), cardiac electrical conduction tracings (electrocardiography), systemic blood pressure (arterial line catheter) and central venous pressure (central venous catheter).

5.9 Inclusion of Precellularized Valves

VIC/EC cross-talk originating from native VICs is well-established as essential to the maintenance of a healthy, quiescent, and non-calcifying valvular endothelium. Co-culture studies[121,122] have shown that in as little as 7 days, the absence of VICs induces pro-fibro-calcific endothelial-to-mesenchymal transition (EMT) in valvular ECs. This in turn drives pathological osteogenesis and calcific nodule formation that causes valvular stenosis *in vivo*. Although in situ reendothelialization may begin within several days of acellular scaffold implantation[123–125], recellularization of the valve leaflet interstitium through native fibroblast-like cell migration and/or differentiation occurs on a much longer timeline[123,125,126]. The majority of rapid cellular infiltration into acellular valvular scaffolds after implantation is derived from circulating cell sources (e.g. myeloid, leukocyte, hematopoietic stem cells, or endothelial progenitor cells[123,127–130]). These circulating cell sources will be absent during REHEART bioreactor pre-conditioning with culture media, and migration/invasion of cells from adjacent engineered tissues into acellular valve scaffolds during bioreactor preconditioning has never been successfully demonstrated. Furthermore, in the absence of cellularization with VICs or VIC-like cells (e.g. MSC), the majority of early host cell invasion is immune/inflammatory in nature[123,128,130]; by pre-cellularizing with hypoimmune VICs we aim to avoid activation of inflammatory processes that could otherwise

challenge the immune-shielded nature of the implanted engineered heart, minimize rejection risk, and instead direct homeostatic scaffold remodeling.

Pre-implantation cellularization with iVICs will ensure the engineered valve tissues take full advantage of bioreactor pre-conditioning periods, and undergo successful iVIC-driven remodeling in preparation to immediately support beneficial valve extracellular matrix homeostasis, remodeling, and tissue robustness when exposed to hemodynamics and pressure gradients in the circulation after heterotopic transplantation. Although replacement-level cardiac output is not immediately necessary after heterotopic transplantation, the engineered valves must immediately operate under typical *in vivo* pressure gradients and cardiac cycles.

5.10 Bi-Ventricular Pacemaker for Electrical Recording and Potential Synchronization

When coupling the engineered heart heterotopically to the native heart, we will use a condition-based criteria to determine whether synchronous contraction is necessary to achieve sufficient cardiac outputs. The decision will be conditional upon the engineered conduction system's ability to consistently self-pace the engineered heart chambers and the digital twin's in silico predictions on combined cardiac output in synchronous and dyssynchronous states. The digital twin's predictions will extend to include the later timepoints when increased cardiac load is placed on the engineered heart (via a reduction in the native heart's venous return).

If synchronization of the engineered and native hearts is necessary, we will implant dual-chamber, bi-ventricular epicardial pacemaker leads on the right atria and ventricles of both hearts, connected to a cardiac resynchronization therapy (CRT) pacer. Spontaneous rhythm from the engineered and native hearts will be recorded. To enable synchronous contraction between the engineered and native hearts, bi-ventricular pacing will provide synchronous pacing of native and bioprinted hearts. This system will also enable testing of the SA node (spontaneous rate and rapid pacing recovery time) and AV node (P-R interval with atrial pacing) constructs. Once engineered heart rhythm and contractility are confirmed, the native heart will be explanted alongside the two leads attached to the native heart. The pacer system will be left on the engineered heart to permit continued evaluation of the bioprinted conduction system constructs and the option to potentially control rhythm via the CRT pacer. With this strategic approach, REHEART is not only able to

provide adequate cardiac output but also record electrical activity via dual-chamber leads, and thus systematically evaluate function of the bioprinted conduction system constructs.

If synchronization between the two hearts is not necessary, dual chamber pacemaker leads will be secured to the epicardium of the engineered right atrium and ventricles. These leads will be used to record electrical conduction traces, including both atrial and ventricular bradyarrhythmias and tachyarrhythmias. The system will serve as a back-up pacing option in support of the engineered conduction system in the event of a failure or delayed maturation. In either the synchronous or dyssynchronous states, the end goal will be a self-pacing orthotopic implant.

5.11 Explant and Postoperative Analysis

Aikawa will supervise all postoperative (histo)pathological studies, assessing explanted bioprinted valve organs vs. native human valve tissues. We will dissect tissue samples (aortic valve, cardiac muscle, vasculature, conduction fiber) from i) explanted bioprinted organs and ii) normal native human tissues (autopsy). These will undergo i) mass spectrometric proteomics to quantify holistic recapitulation of primary human tissue phenotypes, and ii) histological assessment on serial sections via tissue-specific markers (e.g. for valve: OsteoSense, oil Red O, Masson's Trichrome, Movat's Pentachrome, αSMA, CD31, COL1A1) of cell/matrix phenotypes, heterogeneity, and structure followed by quantitative evaluation of all histomorphometry, as we have done previously throughout the heart and vasculature[131–136].

6 References

1. Van Der Linde, D., Konings, E. E. M., Slager, M. A., Witsenburg, M., Helbing, W. A., Takkenberg, J. J. M. & Roos-Hesselink, J. W. Birth prevalence of congenital heart disease worldwide: A systematic review and meta-analysis. *J Am Coll Cardiol* 58, 2241–2247 (2011).

2. Hoffman, J. I. E. & Kaplan, S. The incidence of congenital heart disease. *J Am Coll Cardiol* 39, 1890–1900 (2002).

3. Reller, M. D., Strickland, M. J., Riehle-Colarusso, T., Mahle, W. T. & Correa, A. Prevalence of Congenital Heart Defects in Metropolitan Atlanta, 1998–2005. *J Pediatr* 153, 807 (2008).

4. Gilboa, S. M., Devine, O. J., Kucik, J. E., Oster, M. E., Riehle-Colarusso, T., Nembhard, W. N., Xu, P., Correa, A., Jenkins, K. & Marelli, A. J. Congenital Heart Defects in the United States: Estimating the Magnitude of the Affected Population in 2010. *Circulation* 134, 101–109 (2016).

5. Stallings, E. B., Isenburg, J. L., Rutkowski, R. E., Kirby, R. S., Nembhard, W. N., Sandidge, T., Villavicencio, S., Nguyen, H. H., McMahon, D. M., Nestoridi, E. & Pabst, L. J. National population-based estimates for major birth defects, 2016–2020. *Birth Defects Res* 116, (2024).

6. Mai, C. T., Isenburg, J. L., Canfield, M. A., Meyer, R. E., Correa, A., Alverson, C. J., Lupo, P. J., Riehle-Colarusso, T., Cho, S. J., Aggarwal, D. & Kirby, R. S. National population-based estimates for major birth defects, 2010–2014. *Birth Defects Res* 111, 1420–1435 (2019).

7. Marelli, A. J., Mackie, A. S., Ionescu-Ittu, R., Rahme, E. & Pilote, L. Congenital heart disease in the general population: Changing prevalence and age distribution. *Circulation* 115, 163–172 (2007).

8. Pasquali, S. K., Thibault, D., O'brien, S. M., Jacobs, J. P., Gaynor, J. W., Romano, J. C., Gaies, M., Hill, K. D., Jacobs, M. L., Shahian, D. M., Backer, C. L. & Mayer, J. E. National Variation in Congenital Heart Surgery Outcomes. *Circulation* 142, 1351–1360 (2020).

9. Kumar, S. R., Gaynor, J. W., Jones, L. A., Krohn, C., Mayer, J. E., Nathan, M., O'Brien, J. E., Pizarro, C., Wellnitz, C. & Nelson, J. S. The Society of Thoracic Surgeons Congenital Heart Surgery Database: 2022 Update on Outcomes and Research. *Ann Thorac Surg* 115, 807–819 (2023).

10. Hoffman, J. I. E. & Kaplan, S. The incidence of congenital heart disease. *J Am Coll Cardiol* 39, 1890–1900 (2002).

11. Kumar, S. R., Gaynor, J. W., Jones, L. A., Krohn, C., Mayer, J. E., Nathan, M., O'Brien, J. E., Pizarro, C., Wellnitz, C. & Nelson, J. S. The Society of Thoracic Surgeons Congenital Heart Surgery Database: 2022 Update on Outcomes and Research. *Ann Thorac Surg* 115, 807–819 (2023).

12. Gilboa, S. M., Devine, O. J., Kucik, J. E., Oster, M. E., Riehle-Colarusso, T., Nembhard, W. N., Xu, P., Correa, A., Jenkins, K. & Marelli, A. J. Congenital Heart Defects in the United States: Estimating the Magnitude of the Affected Population in 2010. *Circulation* 134, 101–109 (2016).

13. Fiorentino, F., Stickley, J., Dorobantu, D., Pandey, R., Angelini, G., Barron, D. & Stoica, S. Early Reoperations in a 5-Year National Cohort of Pediatric Patients with Congenital Heart Disease. *Annals of Thoracic Surgery* 101, 1522–1529 (2016).

14. Reller, M. D., Strickland, M. J., Riehle-Colarusso, T., Mahle, W. T. & Correa, A. Prevalence of Congenital Heart Defects in Metropolitan Atlanta, 1998–2005. *J Pediatr* 153, 807 (2008).

15. Garty, Y., Veldtman, G., Lee, K. & Benson, L. Late outcomes after pulmonary valve balloon dilatation in neonates, infants and children. *J Invasive Cardiol* 17, 318–322 (2005).

16. Rao, P. S., Galal, O., Patnana, M., Buck, S. H. & Wilson, A. D. Results of three to 10 year follow up of balloon dilatation of the pulmonary vale. *Heart* 80, 591–595 (1998).

17. Roos-Hesselink, J. W., Meijboom, F. J., Spitaels, S. E. C., VanDomburg, R. T., VanRijen, E. H. M., Utens, E. M. W. J., Bogers, A. J. J. C. & Simoons, M. L. Long-term outcome after surgery for pulmonary stenosis (a longitudinal study of 22-33 years). *Eur Heart J* 27, 482–488 (2006).

18. Hayes, C. J., Gersony, W. M., Driscoll, D. J., Keane, J. F., Kidd, L., O'Fallon, W. M., Pieroni, D. R., Wolfe, R. R. & Weidman, W. H. Second natural history study of congenital heart defects. Results of treatment of patients with pulmonary valvar stenosis. *Circulation* 87, (1993).

19. Earing, M. G., Connolly, H. M., Dearani, J. A., Ammash, N. M., Grogan, M. & Warnes, C. A. Long-term follow-up of patients after surgical treatment for isolated pulmonary valve stenosis. *Mayo Clin Proc* 80, 871–876 (2005).

20. Mayr, B., Vitanova, K., Burri, M., Lang, N., Goppel, G., Voss, B., Lange, R. & Cleuziou, J. Mitral Valve Repair in Children Below Age 10 Years: Trouble or Success? *Annals of Thoracic Surgery* 110, 2082–2087 (2020).

21. Choi, P. S., Sleeper, L. A., Lu, M., Upchurch, P., Baird, C. & Emani, S. M. Revisiting prosthesis choice in mitral valve replacement in children: Durable alternatives to traditional bioprostheses. *Journal of Thoracic and Cardiovascular Surgery* 161, 213-225.e3 (2021).

22. Isaacson, E., Lucjak, C., Johnson, W. K., Yin, Z., Wang, T., Rein, L., Woods, R. K., Tweddell, J. S., Hraska, V. & Mitchell, M. E. Mitral Valve Surgery in Neonates, Infants, and Children: Surgical Approach, Outcomes, and Predictors. *Semin Thorac Cardiovasc Surg* 32, 541–550 (2020).

23. McGurty, D., Remenyi, B., Cheung, M., Engelman, D., Zannino, D., Milne, C., Fittock, M., Steer, A. & Brizard, C. Outcomes After Rheumatic Mitral Valve Repair in Children. *Annals of Thoracic Surgery* 108, 792–797 (2019).

24. Oppido, G., Davies, B., McMullan, D. M., Cochrane, A. D., Cheung, M. M. H., d'Udekem, Y. & Brizard, C. P. Surgical treatment of congenital mitral valve disease: Midterm results of a repair-oriented policy. *Journal of Thoracic and Cardiovascular Surgery* 135, (2008).

25. Romeo, J. L. R., Etnel, J. R. G., Takkenberg, J. J. M., Roos-Hesselink, J. W., Helbing, W. A., van de Woestijne, P., Bogers, A. J. J. C. & Mokhles, M. M. Outcome after surgical repair of tetralogy of Fallot: A systematic review and meta-analysis. *Journal of Thoracic and Cardiovascular Surgery* 159, 220-236.e8 (2020).

26. Normand, S. L. T., Zelevinsky, K., Nathan, M., Abing, H. K., Dearani, J. A., Galantowicz, M., Gaynor, J. W., Habib, R. H., Hanley, F. L., Jacobs, J. P., Kumar, S. R., McDonald, D. E., Pasquali, S. K., Shahian, D. M., Tweddell, J. S., Vener, D. F. & Mayer, J. E. Mortality Prediction After Cardiac Surgery in Children: An STS Congenital Heart Surgery Database Analysis. *Annals of Thoracic Surgery* 114, 785–798 (2022).

27. Buratto, E., Shi, W. Y., Wynne, R., Poh, C. L., Larobina, M., O'Keefe, M., Goldblatt, J., Tatoulis, J. & Skillington, P. D. Improved Survival After the Ross Procedure Compared With Mechanical Aortic Valve Replacement. *J Am Coll Cardiol* 71, 1337–1344 (2018).

28. Danial, P., Neily, A., Pontailler, M., Gaudin, R., Khraiche, D., Osborne-Pellegrin, M., Vouhe, P. & Raisky, O. Ross procedure or complex aortic valve repair using pericardium in children: A real dilemma. *Journal of Thoracic and Cardiovascular Surgery* 163, 1180-1191.e6 (2022).

29. Nelson, J. S., Maul, T. M., Wearden, P. D., Pasquali, S. K. & Romano, J. C. National Practice Patterns and Early Outcomes of Aortic Valve Replacement in Children and Teens. *Annals of Thoracic Surgery* 108, 544–551 (2019).

30. Buratto, E., Hu, T., Lui, A., Wu, D. M., d'Udekem, Y., Brizard, C. P. & Konstantinov, I. E. Early repair of complete atrioventricular septal defect has better survival than staged repair after pulmonary artery banding: A propensity score–matched study. *Journal of Thoracic and Cardiovascular Surgery* 161, 1594–1601 (2021).

31. Chávez, M., Zubair, M. M., Staffa, S. J., Emani, S. M., Quinonez, L. G., Kaza, A., Hoganson, D. M. & Baird, C. W. Primary repair versus pulmonary artery banding in complete atrioventricular canal defects in the modern surgical era. *Journal of Thoracic and Cardiovascular Surgery* 170, 25–33 (2025).

32. Rocha, R. V, Barron, D. J., Mazine, A., Lee, D. S., Fang, J., Silversides, C. K. & Williams, W. G. Evolving concern: Late outcomes after repair of transposition of the great arteries. *Journal of Thoracic and Cardiovascular Surgery* 169, 1296-1303.e2 (2025).

33. Dorobantu, D. M., Pujol, F. E., Kostolny, M., Brown, K. L., Franklin, R. C., Crowe, S., Pagel, C. & Stoica, S. C. Arterial Switch for Transposition of the Great Arteries: Treatment Timing, Late Outcomes, and Risk Factors. *JACC: Advances* 2, (2023).

34. Fricke, T. A., Buratto, E., Weintraub, R. G., Bullock, A., Wheaton, G., Grigg, L., Disney, P., d'Udekem, Y., Brizard, C. P. & Konstantinov, I. E. Long-term outcomes of the arterial switch operation. *Journal of Thoracic and Cardiovascular Surgery* 163, 212–219 (2022).

35. Gellis, L., Binney, G., Alshawabkeh, L., Lu, M., Landzberg, M. J., Mayer, J. E., Mullen, M. P., Valente, A. M., Sleeper, L. A. & Brown, D. W. Long-term fate of the truncal valve. *J Am Heart Assoc* 9, (2020).

36. Naimo, P. S., Bell, D., Fricke, T. A., d'Udekem, Y., Brizard, C. P., Alphonso, N. & Konstantinov, I. E. Truncus arteriosus repair: A 40-year multicenter perspective. *Journal of Thoracic and Cardiovascular Surgery* 161, 230–240 (2021).

37. Balasubramanya, S., Zurakowski, D., Borisuk, M., Kaza, A. K., Emani, S. M., del Nido, P. J. & Baird, C. W. Right ventricular outflow tract reintervention after primary tetralogy of Fallot repair in neonates and young infants. *Journal of Thoracic and Cardiovascular Surgery* 155, 726–734 (2018).

38. Boucek, K., Mastropietro, C. W., Beall, J., Keller, E., Beshish, A., Flores, S., Chlebowski, M., Yates, A. R., Choudhury, T. A., Mueller, D., Kwiatkowski, D. M., Migally, K., Karki, K., Willett, R., Radman, M. R., Reddy, C., Piggott, K., Capone, C. A., Kapileshwarkar, Y., Vijayakumar, N., Prentice, E., Narasimhulu, S. S., Martin, R. H. & Costello, J. M. Staged vs Complete Repair in Tetralogy of Fallot With Pulmonary Atresia. *Annals of Thoracic Surgery* 115, 1463–1468 (2023).

39. Siddeek, H., Lunos, S., Thomas, A. S., McCracken, C., Steinberger, J. & Kochilas, L. Long Term Outcomes of Tetralogy of Fallot With Absent Pulmonary Valve (from the Pediatric Cardiac Care Consortium). *American Journal of Cardiology* 158, 118–123 (2021).

40. Chelliah, A., Moon-Grady, A. J., Peyvandi, S., Chiu, J. S., Bost, J. E., Schidlow, D., Carroll, S. J., Davey, B., Divanovic, A., Hornberger, L., Howley, L. W., Kavanaugh-Mchugh, A., Kovalchin, J. P., Levasseur, S. M., Lindblade, C. L., Morris, S. A., Ngwezi, D., Pruetz, J. D., Puchalski, M. D., Rychik, J., Samai, C., Tacy, T. A., Tworetzky, W., Vernon, M. M., Yeh, J. & Donofrio, M. T. Contemporary outcomes in tetralogy of fallot with absent pulmonary valve after fetal diagnosis. *J Am Heart Assoc* 10, (2021).

41. Goldberg, C. S., Trachtenberg, F., Gaynor, J. W., Mahle, W. T., Ravishankar, C., Schwartz, S. M., Cnota, J. F., Ohye, R. G., Gongwer, R., Taylor, M., Paridon, S., Frommelt, P. C., Afton, K., Atz, A. M., Burns, K. M., Detterich, J. A., Hill, K. D., Cabrera, A. G., Lewis, A. B., Pizarro, C., Shah, A., Sharma, B. & Newburger, J. W. Longitudinal Follow-Up of Children With HLHS and Association Between Norwood Shunt Type and Long-Term Outcomes: The SVR III Study. *Circulation* 148, 1330–1339 (2023).

42. Gaynor, J. W., Mahle, M., Ittenbach, R. F., Kaplinski, M., Lawrence, K. M., Hunt, M. L., Burnham, N. B., Fuller, S., Chen, J. M., Maeda, K., Mavroudis, C. D., Nuri, M. A. K., O'Connor, M. J., Dodds, K. M., Gardner, M. M., Goldberg, D. J., Ravishankar, C., Rychik, J., Kim, Y. Y., Hampton, L., Mascio, C. E., Spray, T. L. & Nicolson, S. C. Long-Term Survival and Patient-Reported Outcomes After Staged Reconstructive Surgery for Hypoplastic Left Heart Syndrome. *J Am Coll Cardiol* 85, 2386–2398 (2025).

43. Li, S., Ma, K., Hu, S., Hua, Z., Yang, K., Yan, J. & Chen, Q. Surgical outcomes of 380 patients with double outlet right ventricle who underwent biventricular repair. *Journal of Thoracic and Cardiovascular Surgery* 148, 817–824 (2014).

44. Holten-Andersen, M., Lippert, M., Holmstrøm, H., Brun, H. & Døhlen, G. Current outcomes of live-born children with double outlet right ventricle in Norway. *European Journal of Cardio-thoracic Surgery* 63, (2023).

45. Oladunjoye, O., Piekarski, B., Baird, C., Banka, P., Marx, G., del Nido, P. J. & Emani, S. M. Repair of double outlet right ventricle: Midterm outcomes. *Journal of Thoracic and Cardiovascular Surgery* 159, 254–264 (2020).

46. Elias, P., Poh, C. L., du Plessis, K., Zannino, D., Rice, K., Radford, D. J., Bullock, A., R.Wheaton, G., Celermajer, D. S. & d'Udekem, Y. Long-term outcomes of single-ventricle palliation for pulmonary atresia with intact ventricular septum: Fontan survivors remain at risk of late myocardial ischaemia and death. *European Journal of Cardio-thoracic Surgery* 53, 1230–1236 (2018).

47. Sukhavasi, A., McHugh-Grant, S., Glatz, A. C., Mondal, A., Griffis, H., Burnham, N., Chen, J. M., Mascio, C. E., Gaynor, J. W., Spray, T. L. & Fuller, S. M. Pulmonary atresia with intact ventricular septum: Intended strategies. *Journal of Thoracic and Cardiovascular Surgery* 164, 1277–1288 (2022).

48. Petit, C. J., Glatz, A. C., Qureshi, A. M., Sachdeva, R., Maskatia, S. A., Justino, H., Goldberg, D. J., Mozumdar, N., Whiteside, W., Rogers, L. S., Nicholson, G. T., McCracken, C., Kelleman, M. & Goldstein, B. H. Outcomes after Decompression of the Right Ventricle in Infants with Pulmonary

Atresia with Intact Ventricular Septum Are Associated with Degree of Tricuspid Regurgitation: Results from the Congenital Catheterization Research Collaborative. *Circ Cardiovasc Interv* 10, (2017).

49. Holst, K. A., Dearani, J. A., Said, S. M., Davies, R. R., Pizarro, C., Knott-Craig, C., Kumar, T. K. S., Starnes, V. A., Kumar, S. R., Pasquali, S. K., Thibault, D. P., Meza, J. M., Hill, K. D., Chiswell, K., Jacobs, J. P. & Jacobs, M. L. Surgical Management and Outcomes of Ebstein Anomaly in Neonates and Infants: A Society of Thoracic Surgeons Congenital Heart Surgery Database Analysis. *Annals of Thoracic Surgery* 106, 785–791 (2018).

50. Sarris, G. E., Giannopoulos, N. M., Tsoutsinos, A. J., Chatzis, A. K., Kirvassilis, G., Brawn, W. J., Comas, J. V, Corno, A. F., Carlo, D. Di, Fragata, J., Hraska, V., Jacobs, J. P., Krupianko, S., Sairanen, H., Stellin, G., Urban, A. & Ziemer, G. Results of surgery for Ebstein anomaly: A multicenter study from the European Congenital Heart Surgeons Association. *Journal of Thoracic and Cardiovascular Surgery* 132, (2006).

51. Eckerström, F., Nyboe, C., Maagaard, M., Redington, A. & Hjortdal, V. E. Survival of patients with congenital ventricular septal defect. *Eur Heart J* 44, 54–61 (2023).

52. Sittiwangkul, R., Azakie, A., Arsdell, G. S. Van, Williams, W. G. & McCrindle, B. W. Outcomes of tricuspid atresia in the Fontan era. *Annals of Thoracic Surgery* 77, 889–894 (2004).

53. Brown, K. L., Huang, Q., Hadjicosta, E., Seale, A. N., Tsang, V., Anderson, D., Barron, D., Bellsham-Revell, H., Pagel, C., Crowe, S., Espuny-Pujol, F., Franklin, R. & Ridout, D. Long-term survival and center volume for functionally single-ventricle congenital heart disease in England and Wales. *Journal of Thoracic and Cardiovascular Surgery* 166, 306-316.e3 (2023).

54. Malhotra, S. P., Lacour-Gayet, F., Campbell, D. N., Miyamoto, S., Clarke, D. R., Dines, M. L., Ivy, D. D. & Mitchell, M. B. Outcomes of Reparative and Transplantation Strategies for Multilevel Left Heart Obstructions With Mitral Stenosis. *Ann Thorac Surg* 86, 1305 (2008).

55. Lee, L. J., Tucker, D. L., Gupta, S., Shaheen, N., Rajeswaran, J., Karamlou, T., Anabila, M., Salam, Y., Ahmad, M., Stewart, R., Pettersson, G. & Najm, H. K. Characterizing the anatomic spectrum, surgical treatment, and long-term clinical outcomes for patients with Shone's syndrome. *Journal of Thoracic and Cardiovascular Surgery* 165, 1224-1234.e9 (2023).

56. Louis, J. D. St., Bannan, M. M., Lutin, W. A. & Wiles, H. B. Surgical Strategies and Outcomes in Patients With Shone Complex: A Retrospective Review. *Annals of Thoracic Surgery* 84, 1357–1363 (2007).

57. Buratto, E., Ye, X. T., Brizard, C. P., Brink, J., d'Udekem, Y. & Konstantinov, I. E. Successful atrioventricular valve repair improves long-term outcomes in children with unbalanced atrioventricular septal defect. *Journal of Thoracic and Cardiovascular Surgery* 154, 2019–2027 (2017).

58. Foker, J. E., Berry, J. M., Vinocur, J. M., Harvey, B. A. & Pyles, L. A. Two-ventricle repairs in the unbalanced atrioventricular canal defect spectrum with midterm follow-up. *Journal of Thoracic and Cardiovascular Surgery* 146, (2013).

59. Nathan, M., Emani, S., IJsselhof, R., Liu, H., Gauvreau, K. & del Nido, P. Mid-term outcomes in unbalanced complete atrioventricular septal defect: role of biventricular conversion from single-ventricle palliation. *European Journal of Cardio-Thoracic Surgery* 52, 565–572 (2017).

60. Binsalamah, Z. M., Ibarra, C., John, R., Zea-Vera, R., Adachi, I., Imamura, M., McKenzie, E. D., Fraser, C. D., Mery, C. M. & Heinle, J. S. Contemporary Midterm Outcomes in Pediatric Patients Undergoing Vascular Ring Repair. *Annals of Thoracic Surgery* 109, 566–572 (2020).

61. Powell, A. J. Vascular Rings and Slings. *Echocardiography in Pediatric and Congenital Heart Disease: From Fetus to Adult: Third Edition* 685–699 (2021). doi:10.1002/9781119612858.CH32

62. Kruse, K., Matsubara, M., Schaeffer, T., Palm, J., Klawonn, F., Osawa, T., Niedermaier, C., Heinisch, P. P., Piber, N., Balling, G., Hager, A., Ewert, P., Horer, J. & Ono, M. Postoperative atrioventricular block after surgery for congenital heart disease: incidence, recovery and risks. *European Journal of Cardio-thoracic Surgery* 67, (2025).

63. Sengupta, A., Gauvreau, K., Kaza, A., Baird, C. W., Schidlow, D. N., del Nido, P. J. & Nathan, M. A Risk Prediction Model for Reintervention After Total Anomalous Pulmonary Venous Connection Repair. *Annals of Thoracic Surgery* 116, 796–802 (2023).

64. Liu, X., Liufu, R., Liu, T., Cen, J., Yu, J., Wen, S., Ou, Y., Chen, J. & Zhuang, J. Supracardiac total anomalous pulmonary venous connection type Ib: Morphology and outcomes. *Journal of Thoracic and Cardiovascular Surgery* 166, 193-200.e1 (2023).

65. Spigel, Z. A., Edmunds, E. E., Caldarone, C. A., Hickey, E. J., Binsalamah, Z. M. & Heinle, J. S. Total anomalous pulmonary venous connection: Influence of heterotaxy and venous obstruction on outcomes. *J Thorac Cardiovasc Surg* 163, 387-395.e3 (2022).

66. Seale, A. N., Uemura, H., Webber, S. A., Partridge, J., Roughton, M., Ho, S. Y., McCarthy, K. P., Jones, S., Shaughnessy, L., Sunnegardh, J., Hanseus, K., Berggren, H., Johansson, S., Rigby, M. L., Keeton, B. R. & Daubeney, P. E. F. Total anomalous pulmonary venous connection: Morphology and outcome from an international population-based study. *Circulation* 122, 2718–2726 (2010).

67. McElhinney, D. B., Asija, R., Zhang, Y., Jaggi, A., Shek, J., Peng, L. F., Boltz, M. G., Ma, M., Martin, E. & Hanley, F. L. 20-Year Experience With Repair of Pulmonary Atresia or Stenosis and Major Aortopulmonary Collateral Arteries. *J Am Coll Cardiol* 82, 1206–1222 (2023).

68. Lurie, I. W., Kappetein, A. P., Loffredo, C. A. & Ferencz, C. Non-cardiac malformations in individuals with outflow tract defects of the heart: The Baltimore-Washington Infant Study (1981-1989). *Am J Med Genet* 59, 76–84 (1995).

69. O'Leary, E. T., Feins, E. N., Davee, J., Baird, C. W., Beroukhim, R., del Nido, P. J., Dionne, A., Gauvreau, K., Hoganson, D. M., Triedman, J. K., Walsh, E. P., Nathan, M., Emani, S. M. & DeWitt, E. S. Intraoperative Conduction Mapping to Reduce Postoperative Atrioventricular Block in Complex Congenital Heart Disease. *J Am Coll Cardiol* 84, 2102–2112 (2024).

70. Zhang, W., Gauvreau, K., DeWitt, E. S., Lee, J. M., Liu, H., Feins, E. N., Kaza, A. K., del Nido, P. J. & Nathan, M. Impact of permanent pacemaker for iatrogenic atrioventricular block on outcomes after congenital heart surgery. *Journal of Thoracic and Cardiovascular Surgery* 169, 411-419.e5 (2025).

71. O'Connor, M., Well, A., Fenrich, A., Venardos, N. M., Shmorhun, D., Mery, C. M. & Fraser, C. D. Incidence and Outcomes of Iatrogenic Complete Atrioventricular Block After Congenital Heart Surgery. *Annals of Thoracic Surgery* 119, 586–593 (2025).

72. Riggs, K. W., Zafar, F., Lorts, A., Chin, C., Bryant, R., Tweddell, J. S. & Morales, D. L. S. The reality of limping to pediatric heart transplantation. *Journal of Thoracic and Cardiovascular Surgery* 159, 2418-2425.e1 (2020).

73. Sharaf, O. M., Bilgili, A., Brennan, Z., Treffalls, J. A., Peek, G. J., Bleiweis, M. S. & Jacobs, J. P. Analysis of UNOS: Pediatric Heart Transplantation Over 36 Years and Contemporary Volume-Outcome Relationship. *Annals of Thoracic Surgery* 118, 1288–1298 (2024).

74. Huebler, M., Schubert, S., Lehmkuhl, H. B., Weng, Y., Miera, O., Alexi-Meskishvili, V., Berger, F. & Hetzer, R. Pediatric heart transplantation: 23-year single-center experience. *European Journal of Cardio-thoracic Surgery* 39, (2011).

75. Egbe, A. C., Miranda, W. R., Jain, C. C., Bonnichsen, C. R., Anderson, J. H., Dearani, J. A., Warnes, C. A., Crestanello, J. & Connolly, H. M. Incidence and Outcomes of Advanced Heart Failure in Adults with Congenital Heart Disease. *Circ Heart Fail* 15, E009675 (2022).

76. Gravina, A., Tediashvili, G., Zheng, Y., Iwabuchi, K. A., Peyrot, S. M., Roodsari, S. Z., Gargiulo, L., Kaneko, S., Osawa, M., Schrepfer, S. & Deuse, T. Synthetic immune checkpoint engagers protect HLA-deficient iPSCs and derivatives from innate immune cell cytotoxicity. *Cell Stem Cell* 30, 1538-1548.e4 (2023).

77. Deuse, T., Hu, X., Agbor-Enoh, S., Jang, M. K., Alawi, M., Saygi, C., Gravina, A., Tediashvili, G., Nguyen, V. Q., Liu, Y., Valantine, H., Lanier, L. L. & Schrepfer, S. The SIRPα-CD47 immune checkpoint in NK cells. *Journal of Experimental Medicine* 218, (2021).

78. Han, X., Wang, M., Duan, S., Franco, P. J., Kenty, J. H. R., Hedrick, P., Xia, Y., Allen, A., Ferreira, L. M. R., Strominger, J. L., Melton, D. A., Meissner, T. B. & Cowan, C. A. Generation of hypoimmunogenic human pluripotent stem cells. *Proc Natl Acad Sci U S A* 116, 10441–10446 (2019).

79. Lee, U., Zhang, Y., Zhu, Y., Luo, A. C., Gong, L., Tremmel, D. M., Kim, Y., Villarreal, V. S., Wang, X., Lin, R. Z., Cui, M., Ma, M., Yuan, K., Wang, K., Chen, K. & Melero-Martin, J. M. Robust differentiation of human pluripotent stem cells into mural progenitor cells via transient activation of NKX3.1. *Nature Communications* 15, (2024).

80. Wang, K., Lin, R. Z., Hong, X., Ng, A. H., Lee, C. N., Neumeyer, J., Wang, G., Wang, X., Ma, M., Pu, W. T., Church, G. M. & Melero-Martin, J. M. Robust differentiation of human pluripotent stem cells into endothelial cells via temporal modulation of ETV2 with modified mRNA. *Sci Adv* 6, (2020).

81. Pasqualini, F. S., Sheehy, S. P., Agarwal, A., Aratyn-Schaus, Y. & Parker, K. K. Structural phenotyping of stem cell-derived cardiomyocytes. *Stem Cell Reports* 4, 340–347 (2015).

82. Prondzynski, M., Berkson, P., Trembley, M. A., Tharani, Y., Shani, K., Bortolin, R. H., Sweat, M. E., Mayourian, J., Yucel, D., Cordoves, A. M., Gabbin, B., Hou, C., Anyanwu, N. J., Nawar, F., Cotton, J., Milosh, J., Walker, D., Zhang, Y., Lu, F., Liu, X., Parker, K. K., Bezzerides, V. J. & Pu, W. T. Efficient and reproducible generation of human iPSC-derived cardiomyocytes and cardiac organoids in stirred suspension systems. *Nat Commun* 15, (2024).

83. Wang, G., McCain, M. L., Yang, L., He, A., Pasqualini, F. S., Agarwal, A., Yuan, H., Jiang, D., Zhang, D., Zangi, L., Geva, J., Roberts, A. E., Ma, Q., Ding, J., Chen, J., Wang, D. Z., Li, K., Wang, J., Wanders, R. J. A., Kulik, W., Vaz, F. M., Laflamme, M. A., Murry, C. E., Chien, K. R.,

Kelley, R. I., Church, G. M., Parker, K. K. & Pu, W. T. Modeling the mitochondrial cardiomyopathy of Barth syndrome with induced pluripotent stem cell and heart-on-chip technologies. *Nat Med* 20, 616–623 (2014).

84. Park, S.-J., Zhang, D., Qi, Y., Li, Y., Lee, K. Y., Bezzerides, V. J., Yang, P., Xia, S., Kim, S. L., Liu, X., Lu, F., Pasqualini, F. S., Campbell, P. H., Geva, J., Roberts, A. E., Kleber, A. G., Abrams, D. J., Pu, W. T. & Parker, K. K. Insights Into the Pathogenesis of Catecholaminergic Polymorphic Ventricular Tachycardia From Engineered Human Heart Tissue. *Circulation* 140, 390–404 (2019).

85. Alford, P. W., Feinberg, A. W., Sheehy, S. P. & Parker, K. K. Biohybrid thin films for measuring contractility in engineered cardiovascular muscle. *Biomaterials* 31, 3613–3621 (2010).

86. Park, S. J., Zhang, D., Qi, Y., Li, Y., Lee, K. Y., Bezzerides, V. J., Yang, P., Xia, S., Kim, S. L., Liu, X., Lu, F., Pasqualini, F. S., Campbell, P. H., Geva, J., Roberts, A. E., Kleber, A. G., Abrams, D. J., Pu, W. T. & Parker, K. K. Insights Into the Pathogenesis of Catecholaminergic Polymorphic Ventricular Tachycardia From Engineered Human Heart Tissue. *Circulation* 140, 390–404 (2019).

87. Sheehy, S. P., Pasqualini, F., Grosberg, A., Park, S. J., Aratyn-Schaus, Y. & Parker, K. K. Quality metrics for stem cell-derived cardiac myocytes. *Stem Cell Reports* 2, 282–294 (2014).

88. Capulli, A. K., Emmert, M. Y., Pasqualini, F. S., Kehl, D., Caliskan, E., Lind, J. U., Sheehy, S. P., Park, S. J., Ahn, S., Weber, B., Goss, J. A., Hoerstrup, S. P. & Parker, K. K. JetValve: Rapid manufacturing of biohybrid scaffolds for biomimetic heart valve replacement. *Biomaterials* 133, 229–241 (2017).

89. Macqueen, L. A., Sheehy, S. P., Chantre, C. O., Zimmerman, J. F., Pasqualini, F. S., Liu, X., Goss, J. A., Campbell, P. H., Gonzalez, G. M., Park, S.-J., Capulli, A. K., Ferrier, J. P., Fettah Kosar, T., Mahadevan, L., Pu, W. T. & Parker, K. K. A tissue-engineered scale model of the heart ventricle. *Nat Biomed Eng* 2, 930–941 (2018).

90. Motta, S., Peters, M., Chantre, C., Chang, H., Cera, L., Liu, Q., Cordoves, E., Fioretta, E., Zaytseva, P., Cesarovic, N., Emmert, M., Hoerstrup, S. & Parker, K. K. On-demand heart valve manufacturing using focused rotary jet spinning. *Matter* 6, 1860–1879 (2023).

91. Chang, H., Liu, Q., Zimmerman, J. F., Lee, K. Y., Jin, Q., Peters, M. M., Rosnach, M., Choi, S., Kim, S. L., Ann, H., Ardoña, M., Macqueen, L. A., Chantre, C. O., Motta, S. E., Cordoves, E. M. & Parker, K. K. Recreating the heart's helical structure-function relationship with focused rotary jet spinning. *Science* 377, 180–185 (2022).

92. Choi, S., Lee, K. Y., Kim, S. L., MacQueen, L. A., Chang, H., Zimmerman, J. F., Jin, Q., Peters, M. M., Ardoña, H. A. M., Liu, X., Heiler, A. C., Gabardi, R., Richardson, C., Pu, W. T., Bausch, A. R. & Parker, K. K. Fibre-infused gel scaffolds guide cardiomyocyte alignment in 3D-printed ventricles. *Nat Mater* 22, 1039–1046 (2023).

93. Holzapfel, G. A. & Ogden, R. W. Constitutive modelling of passive myocardium: a structurally based framework for material characterization. *Philos Trans A Math Phys Eng Sci* 367, 3445–3475 (2009).

94. Marié, S., Ricot, D. & Sagaut, P. Comparison between lattice Boltzmann method and Navier-Stokes high order schemes for computational aeroacoustics. *J Comput Phys* 228, 1056–1070 (2009).

95. Aono, H., Gupta, A., Qi, D. & Shyy, W. The lattice Boltzmann method for flapping wing aerodynamics. *40th AIAA Fluid Dynamics Conference* 1–27 (2010). doi:10.2514/6.2010-4867

96. Wiputra, H., Lai, C. Q., Lim, G. L., Heng, J. J. W., Guo, L., Soomar, S. M., Leo, H. L., Biwas, A., Mattar, C. N. Z. & Yap, C. H. Fluid mechanics of human fetal right ventricles from image-based computational fluid dynamics using 4D clinical ultrasound scans. *Am J Physiol Heart Circ Physiol* 311, H1498–H1508 (2016).

97. Wiputra, H., Chen, C. K., Talbi, E., Lim, G. L., Soomar, S. M., Biswas, A., Mattar, C. N. Z., Bark, D., Leo, H. L. & Yap, C. H. Human fetal hearts with tetralogy of Fallot have altered fluid dynamics and forces. *Am J Physiol Heart Circ Physiol* 315, H1649–H1659 (2018).

98. Green, L., Chan, W. X., Ren, M., Mattar, C. N. Z., Lee, L. C. & Yap, C. H. The dependency of fetal left ventricular biomechanics function on myocardium helix angle configuration. *Biomech Model Mechanobiol* 22, 629–643 (2023).

99. Wong, H. S., Wiputra, H., Tulzer, A., Tulzer, G. & Yap, C. H. Fluid Mechanics of Fetal Left Ventricle During Aortic Stenosis with Evolving Hypoplastic Left Heart Syndrome. *Ann Biomed Eng* 50, 1158–1172 (2022).

100. Pervolaraki, E., Hodgson, S., Holden, A. V & Benson, A. P. Towards computational modelling of the human foetal electrocardiogram: Normal sinus rhythm and congenital heart block. *Europace* 16, 758–765 (2014).

101. Biktasheva, I. V, Anderson, R. A., Holden, A. V, Pervolaraki, E. & Wen, F. C. Cardiac re-entry dynamics and self-termination in DT-MRI based model of human fetal heart. *Front Phys* 5, 327090 (2018).

102. Zebhi, B., Wiputra, H., Howley, L., Cuneo, B., Park, D., Hoffman, H., Gilbert, L., Yap, C. H. & Bark, D. Right ventricle in hypoplastic left heart syndrome exhibits altered hemodynamics in the human fetus. *J Biomech* 112, (2020).

103. Kléber, A. G. & Rudy, Y. Basic Mechanisms of Cardiac Impulse Propagation and Associated Arrhythmias. *Physiol Rev* 84, 431–488 Preprint at https://doi.org/10.1152/physrev.00025.2003 (2004)

104. Fedorov, V. V, Glukhov, A. V, Chang, R., Kostecki, G., Aferol, H., Hucker, W. J., Wuskell, J. P., Loew, L. M., Schuessler, R. B., Moazami, N. & Efimov, I. R. Optical mapping of the isolated coronary-perfused human sinus node. *J Am Coll Cardiol* 56, 1386–1394 (2010).

105. Lee, K. Y., Park, S.-J., Matthews, D. G., Kim, S. L., Marquez, C. A., Zimmerman, J. F., Ardoña, H. A. M., Kleber, A. G., Lauder, G. V & Parker, K. K. An autonomously swimming biohybrid fish designed with human cardiac biophysics. *Science* 375, 639–647 (2022).

106. Wang, Q., Yang, H., Bai, A., Jiang, W., Li, X., Wang, X., Mao, Y., Lu, C., Qian, R., Guo, F., Ding, T., Chen, H., Chen, S., Zhang, J., Liu, C. & Sun, N. Functional engineered human cardiac patches prepared from nature's platform improve heart function after acute myocardial infarction. *Biomaterials* 105, 52–65 (2016).

107. Rohr, S., Kucera, J. P., Fast, V. G. & Kléber, A. G. Paradoxical improvement of impulse conduction in cardiac tissue by partial cellular uncoupling. *Science* 275, 841–844 (1997).

108. Peters, M. M., Brister, J. K., Tang, E. M., Zhang, F. W., Lucian, V. M., Trackey, P. D., Bone, Z., Zimmerman, J. F., Jin, Q., Burpo, F. J. & Parker, K. K. Self-organizing behaviors of cardiovascular cells on synthetic nanofiber scaffolds. *APL Bioeng* 7, 46114 (2023).

109. Lopez-Moya, M., Melgar-Lesmes, P., Kolandaivelu, K., De La Torre Hernández, J. M., Edelman, E. R. & Balcells, M. Optimizing Glutaraldehyde-Fixed Tissue Heart Valves with Chondroitin Sulfate Hydrogel for Endothelialization and Shielding against Deterioration. *Biomacromolecules* 19, 1234–1244 (2018).

110. Zhou, Y., Yan, G., Wen, S., Yim, W. Y., Wang, Z., Chen, X., Xu, Y., Chen, X., Cao, H., Bai, P., Li, F., Shi, J., Wang, J., Qiao, W. & Dong, N. Nitric Oxide Generation and Endothelial Progenitor Cells Recruitment for Improving Hemocompatibility and Accelerating Endothelialization of Tissue Engineering Heart Valve. *Adv Funct Mater* 33, 2211267 (2023).

111. Driscoll, K., Cruz, A. D. & Butcher, J. T. Inflammatory and Biomechanical Drivers of Endothelial-Interstitial Interactions in Calcific Aortic Valve Disease. *Circ Res* 128, 1344–1370 (2021).

112. Butcher, J. T., Tressel, S., Johnson, T., Turner, D., Sorescu, G., Jo, H. & Nerem, R. M. Transcriptional profiles of valvular and vascular endothelial cells reveal phenotypic differences: Influence of shear stress. *Arterioscler Thromb Vasc Biol* 26, 69–77 (2006).

113. Zhang, H., Lui, K. O. & Zhou, B. Endocardial cell plasticity in cardiac development, diseases and regeneration. *Circ Res* 122, 774–789 (2018).

114. Liu, C. Z., Prasad, A., Jadhav, B., Liu, Y., Gu, M., Sharp, A. J. & Gelb, B. D. Feeder-free generation and characterization of endocardial and cardiac valve cells from human pluripotent stem cells. *iScience* 27, 108599 (2024).

115. Cheng, L. X., Xie, M. H., Qiao, W. H., Song, Y., Zhang, Y. Y., Geng, Y. C., Xu, W. L., Wang, L., Wang, Z., Huang, K., Dong, N. G. & Sun, Y. H. Generation and characterization of cardiac valve endothelial-like cells from human pluripotent stem cells. *Commun Biol* 4, 1–15 (2021).

116. Cai, Z., Zhu, M., Xu, L., Wang, Y., Xu, Y., Yim, W. Y., Cao, H., Guo, R., Qiu, X., He, X., Shi, J., Qiao, W. & Dong, N. Directed Differentiation of Human Induced Pluripotent Stem Cells to Heart Valve Cells. *Circulation* 149, 1435–1456 (2024).

117. Harding, J., Vintersten-Nagy, K., Yang, H., Tang, J. K., Shutova, M., Jong, E. D., Lee, J. H., Massumi, M., Oussenko, T., Izadifar, Z., Zhang, P., Rogers, I. M., Wheeler, M. B., Lye, S. J., Sung, H. K., Li, C. J., Izadifar, M. & Nagy, A. Immune-privileged tissues formed from immunologically cloaked mouse embryonic stem cells survive long term in allogeneic hosts. *Nat Biomed Eng* 8, 427–442 (2024).

118. Hu, X., Gattis, C., Olroyd, A. G., Friera, A. M., White, K., Young, C., Basco, R., Lamba, M., Wells, F., Ankala, R., Dowdle, W. E., Lin, A., Egenberger, K., Rukstalis, J. M., Millman, J. R., Connolly, A. J., Deuse, T. & Schrepfer, S. Human hypoimmune primary pancreatic islets avoid rejection and autoimmunity and alleviate diabetes in allogeneic humanized mice. *Sci Transl Med* 15, (2023).

119. Luo, A. C., Wang, J., Wang, K., Zhu, Y., Gong, L., Lee, U., Li, X., Tremmel, D. M., Lin, R. Z., Ingber, D. E., Gorman, J. & Melero-Martin, J. M. A streamlined method to generate endothelial cells from human pluripotent stem cells via transient doxycycline-inducible ETV2 activation. *Angiogenesis* (2024). doi:10.1007/s10456-024-09937-5

120. Wang, K., Lin, R. Z., Hong, X., Ng, A. H., Lee, C. N., Neumeyer, J., Wang, G., Wang, X., Ma, M., Pu, W. T., Church, G. M. & Melero-Martin, J. M. Robust differentiation of human pluripotent stem cells into endothelial cells via temporal modulation of ETV2 with modified mRNA. *Sci Adv* 6, (2020).

121. Hjortnaes, J., Shapero, K., Goettsch, C., Hutcheson, J. D., Keegan, J., Kluin, J., Mayer, J. E., Bischoff, J. & Aikawa, E. Valvular interstitial cells suppress calcification of valvular endothelial cells. *Atherosclerosis* 242, 251–260 (2015).

122. Gee, T., Farrar, E., Wang, Y., Wu, B., Hsu, K., Zhou, B. & Butcher, J. NFκB (Nuclear Factor κ-Light-Chain Enhancer of Activated B Cells) Activity Regulates Cell-Type-Specific and Context-Specific Susceptibility to Calcification in the Aortic Valve. *Arterioscler Thromb Vasc Biol* 40, 638–655 (2020).

123. Yacoub, M. H., Tseng, Y. T., Kluin, J., Vis, A., Stock, U., Smail, H., Sarathchandra, P., Aikawa, E., El-Nashar, H., Chester, A. H., Shehata, N., Nagy, M., El-sawy, A., Li, W., Burriesci, G., Salmonsmith, J., Romeih, S. & Latif, N. Valvulogenesis of a living, innervated pulmonary root induced by an acellular scaffold. *Commun Biol* 6, 1–15 (2023).

124. Lichtenberg, A., Tudorache, I., Cebotari, S., Ringes-Lichtenberg, S., Sturz, G., Hoeffler, K., Hurscheler, C., Brandes, G., Hilfiker, A. & Haverich, A. In vitro re-endothelialization of detergent decellularized heart valves under simulated physiological dynamic conditions. *Biomaterials* 27, 4221–4229 (2006).

125. Ota, T., Sawa, Y., Iwai, S., Kitajima, T., Ueda, Y., Coppin, C., Matsuda, H. & Okita, Y. Fibronectin-hepatocyte growth factor enhances reendothelialization in tissue-engineered heart valve. *Annals of Thoracic Surgery* 80, 1794–1801 (2005).

126. Baraki, H., Tudorache, I., Braun, M., Höffler, K., Görler, A., Lichtenberg, A., Bara, C., Calistru, A., Brandes, G., Hewicker-Trautwein, M., Hilfiker, A., Haverich, A. & Cebotari, S. Orthotopic replacement of the aortic valve with decellularized allograft in a sheep model. *Biomaterials* 30, 6240–6246 (2009).

127. Flameng, W., De Visscher, G., Mesure, L., Hermans, H., Jashari, R. & Meuris, B. Coating with fibronectin and stromal cell-derived factor-1α of decellularized homografts used for right ventricular outflow tract reconstruction eliminates immune response-related degeneration. *Journal of Thoracic and Cardiovascular Surgery* 147, (2014).

128. De Kort, B. J., Marzi, J., Brauchle, E. M., Lichauco, A. M., Bauer, H. S., Serrero, A., Dekker, S., Cox, M. A. J., Schoen, F. J., Schenke-Layland, K., Bouten, C. V. C. & Smits, A. I. P. M. Inflammatory and regenerative processes in bioresorbable synthetic pulmonary valves up to two years in sheep–Spatiotemporal insights augmented by Raman microspectroscopy. *Acta Biomater* 135, 243–259 (2021).

129. Williams, J. K., Miller, E. S., Lane, M. R., Atala, A., Yoo, J. J. & Jordan, J. E. Characterization of CD133 Antibody-Directed Recellularized Heart Valves. *J Cardiovasc Transl Res* 8, 411–420 (2015).

130. Motta, S. E., Fioretta, E. S., Lintas, V., Dijkman, P. E., Hilbe, M., Frese, L., Cesarovic, N., Loerakker, S., Baaijens, F. P. T., Falk, V., Hoerstrup, S. P. & Emmert, M. Y. Geometry influences

inflammatory host cell response and remodeling in tissue-engineered heart valves in-vivo. *Sci Rep* 10, 19882 (2020).

131. Clift, C. L., Blaser, M. C., Gerrits, W., Turner, M. E., Sonawane, A., Pham, T., Andresen, J. L., Fenton, O. S., Grolman, J. M., Campedelli, A., Buffolo, F., Schoen, F. J., Hjortnaes, J., Muehlschlegel, J. D., Mooney, D. J., Aikawa, M., Singh, S. A., Langer, R. & Aikawa, E. Intracellular proteomics and extracellular vesiculomics as a metric of disease recapitulation in 3D-bioprinted aortic valve arrays. *Sci Adv* 10, 9793 (2024).

132. Decano, J. L., Iwamoto, Y., Goto, S., Lee, J. Y., Matamalas, J. T., Halu, A., Blaser, M., Lee, L. H., Pieper, B., Chelvanambi, S., Silva-Nicolau, J., Bartoli-Leonard, F., Higashi, H., Shibata, H., Vyas, P., Wang, J., Gostjeva, E., Body, S. C., Singh, S. A., Aikawa, M. & Aikawa, E. A disease-driver population within interstitial cells of human calcific aortic valves identified via single-cell and proteomic profiling. *Cell Rep* 39, (2022).

133. Iqbal, F., Schlotter, F., Becker-Greene, D., Lupieri, A., Goettsch, C., Hutcheson, J. D., Rogers, M. A., Itoh, S., Halu, A., Lee, L. H., Blaser, M. C., Mlynarchik, A. K., Hagita, S., Kuraoka, S., Chen, H. Y., Engert, J. C., Passos, L. S. A., Jha, P. K., Osborn, E. A., Jaffer, F. A., Body, S. C., Robson, S. C., Thanassoulis, G., Aikawa, M., Singh, S. A., Sonawane, A. R. & Aikawa, E. Sortilin enhances fibrosis and calcification in aortic valve disease by inducing interstitial cell heterogeneity. *Eur Heart J* 44, 885–898 (2023).

134. Blaser, M. C., Buffolo, F., Halu, A., Turner, M. E., Schlotter, F., Higashi, H., Pantano, L., Clift, C. L., Saddic, L. A., Atkins, S. K., Rogers, M. A., Pham, T., Vromman, A., Shvartz, E., Sukhova, G. K., Monticone, S., Camussi, G., Robson, S. C., Body, S. C., Muehlschlegel, J. D., Singh, S. A., Aikawa, M. & Aikawa, E. Multiomics of Tissue Extracellular Vesicles Identifies Unique Modulators of Atherosclerosis and Calcific Aortic Valve Stenosis. *Circulation* 148, 661–678 (2023).

135. Schlotter, F., Halu, A., Goto, S., Blaser, M. C., Body, S. C., Lee, L. H., Higashi, H., Delaughter, D. M., Hutcheson, J. D., Vyas, P., Pham, T., Rogers, M. A., Sharma, A., Seidman, C. E., Loscalzo, J., Seidman, J. G., Aikawa, M., Singh, S. A. & Aikawa, E. Spatiotemporal multi-omics mapping generates a molecular atlas of the aortic valve and reveals networks driving disease. *Circulation* 138, 377–393 (2018).

136. Hutcheson, J. D., Goettsch, C., Bertazzo, S., Maldonado, N., Ruiz, J. L., Goh, W., Yabusaki, K., Faits, T., Bouten, C., Franck, G., Quillard, T., Libby, P., Aikawa, M., Weinbaum, S. & Aikawa, E. Genesis and growth of extracellular-vesicle-derived microcalcification in atherosclerotic plaques. *Nat Mater* 15, 335–343 (2016).

137. Copeland, J. & Copeland, H. Heterotopic Heart Transplantation: Technical Considerations. *Operative Techniques in Thoracic and Cardiovascular Surgery* 21, 269–280 (2016).

138. Novitzky, D., Cooper, D. K. C. & Barnard, C. N. The surgical technique of heterotopic heart transplantation. *Ann Thorac Surg* 36, 476–482 (1983).